



Article

Developing and Using Empirical Bio-Optical Algorithms in the Western Part of the Bering Sea in the Late Summer Season

Pavel A. Salyuk^{1,*}, Igor E. Stepochkin¹, Ekaterina B. Sokolova¹, Svetlana P. Pugach¹, Vasiliy A. Kachur² and Irina I. Pipko¹

¹ V.I. Il'ichev Pacific Oceanological Institute, Far Eastern Branch, Russian Academy of Science (POI FEB RAS), 690041 Vladivostok, Russia

² Institute of Automation and Control Processes, Far Eastern Federal University, 690922 Vladivostok, Russia

* Correspondence: psalyuk@poi.dvo.ru

Abstract: This study aimed to assess the applicability of global bio-optical algorithms for the estimation of chlorophyll-a (chl-a) concentration (C) and develop regional empirical bio-optical algorithms for estimating C and colored dissolved organic matter (CDOM) content (D) from ocean remote sensing reflectance spectra in the western part of the Bering Sea in the late summer period. The analysis took into account possible problems with the different relative contributions of phytoplankton and CDOM to water-leaving radiance and possible errors associated with the atmosphere correction procedure for ocean color satellite data. Shipborne remote sensing measurements obtained using an above-water hyperspectral ASD HandHeld spectroradiometer, satellite measurements collected via MODIS and VIIRS radiometers, and in situ measurements of C and D in seawater were used. The simulated values of the different multispectral satellite radiometers with daily or 2-day global coverage, obtained by applying the corresponding spectral response functions to ship hyperspectral data, were also analyzed. In this paper, a list of recommended regional bio-optical algorithms is presented. Recommendations are given depending on the possible quality of atmospheric correction and the purpose of use. To obtain more precise estimations of C , OC3/OC4-like algorithms should be used. If the atmosphere correction is poor, then use OC2-like algorithms in which spectral bands in the 476–539 nm range should be used to estimate C and bands near 443 nm to estimate D ; however, in the last case, this will provide only the order of magnitude. To estimate more independent fields of C and D , it is necessary to use a spectral range of 501–539 nm for chl-a and bands near 412 nm in the case of modern satellite radiometers (e.g., OLCI or SGLI), for which this band is not the first. Additionally, we showed that global bio-optical algorithms can be applied with acceptable accuracy and similar recommendations.



Citation: Salyuk, P.A.; Stepochkin, I.E.; Sokolova, E.B.; Pugach, S.P.; Kachur, V.A.; Pipko, I.I. Developing and Using Empirical Bio-Optical Algorithms in the Western Part of the Bering Sea in the Late Summer Season. *Remote Sens.* **2022**, *14*, 5797. <https://doi.org/10.3390/rs14225797>

Academic Editor: Chung-Ru Ho

Received: 21 October 2022

Accepted: 11 November 2022

Published: 16 November 2022

Publisher's Note: MDPI stays neutral with regard to jurisdictional claims in published maps and institutional affiliations.



Copyright: © 2022 by the authors. Licensee MDPI, Basel, Switzerland. This article is an open access article distributed under the terms and conditions of the Creative Commons Attribution (CC BY) license (<https://creativecommons.org/licenses/by/4.0/>).

Keywords: chlorophyll-a; colored dissolved organic matter; remote sensed reflectance; spectral response function; hyperspectral; multispectral; band ratio index; Anadyr Bay; Anadyr River

1. Introduction

The western part of the Bering Sea is a highly dynamic, nutrient-rich, and highly productive region that is also influenced by the flow of the Anadyr River. Therefore, various natural processes determine the variability of phytoplankton and colored dissolved organic matter (CDOM) content in the seawater, which changes the color of that part of the Bering Sea. It is important to develop remote sensing approaches that allow for the accurate calculation of chlorophyll-a (chl-a)—the main pigment of phytoplankton—concentration and CDOM content, independent of the presence of in situ observations and with a minimal influence of these parameters on each other.

There are two main approaches to the estimation of chl-a concentration and CDOM content in seawater using optical remote sensing and bio-optical algorithms. The empirical method uses experimentally obtained ratios between the remote sensing reflectance (R_{rs}) at

specific wavelengths and some values, which characterize the optically active constituent (OAC) content of seawater [1,2]. In contrast, in the semi-analytical method, the spectral distribution of the Rrs is fitted as a function of the scattering and absorption coefficients of the OACs [3].

The above methods have their advantages and disadvantages [4]. In two previously published papers [5,6], significant errors were obtained using empirical bio-optical algorithms when the ratio between chl-a and CDOM differed significantly from that used to derive the Rrs. To solve this problem, it is necessary to obtain many measurements using direct methods to accumulate sufficient statistics and build algorithms for the different regions and seasons, as shown in the works [7–10]. The disadvantages of semi-analytical bio-optical algorithms include its sensitivity to atmospheric correction errors [11,12], the need for large computational resources, and the instability of the inverse problem decision, which leads to a radically erroneous result in the wrong local minimum [13]. Moreover, in simple optical cases, the extra complexity of this approach can lead to additional errors [5].

The overlapping of the spectral signatures of the absorption and scattering coefficients of seawater and its constituents is a problem common to both the empirical and semi-analytical approaches. This issue is especially noticeable when the spectral values of different OACs are comparable in magnitude and the ratios of the OAC concentrations are different [14,15]. It should be noted that the ratio of chl-a to CDOM content may depend on various factors including the presence of allochthonous dissolved organic matter (DOM), which adds to the total CDOM content; the degradation of CDOM molecules, which leads to a change in the spectral characteristics of light absorption by CDOM; and the functional state or species composition of phytoplankton, which affect the spectra of light absorption by phytoplankton and/or the content of chl-a inside the cells. These factors vary from region to region and season to season [16,17].

The semi-analytical approach is more promising since it is less sensitive to variations in the OAC ratios. Furthermore, it is expected that its limitations can be reduced by the increase in computing power, the improvement in the spectral resolution of remote sensing, and the development of new regional absorption and scattering models. Nevertheless, the empirical approaches are still applicable [18]. They are more independent of the atmospheric correction errors than semi-analytical methods [12] and can be used to determine the initial and boundary conditions of semi-analytical bio-optical models or to check if semi-analytical algorithms can be used to obtain the correct solutions. The careful selection of the spectral ranges that will maximally separate the contributions of OACs to the seawater Rrs spectra is one way to improve empirical bio-optical algorithms.

This work aimed to check the applicability of global bio-optical algorithms for the estimation of chlorophyll-a (chl-a) concentration and to develop empirical bio-optical algorithms for estimating chl-a concentration and CDOM content from Rrs spectra in the western part of the Bering Sea, taking into account possible problems with the atmosphere correction algorithm and the different relative contributions of phytoplankton and CDOM into the water-leaving radiance.

2. Study Area

The experimental data analyzed in the present paper were collected during an expedition on the oceanic vessel “Professor Khljustin” in the western part of the Bering Sea in August 2013 (Figure 1). The circles in Figures 1 and 2 indicate the locations of the simultaneous in situ and shipboard remote sensing measurements. In addition, an image of the averaged satellite estimates of chl-a concentration (from MODIS-Aqua measurements for August in the period 2002–2020 [19]) is shown in Figure 1, while the averaged northward velocity of the sea surface current (from CMEMS global ocean eddy-resolving reanalysis for August 2013 [20]) is illustrated in Figure 2. The classification of the obtained points and the corresponding color designations are presented in Section 4.2.

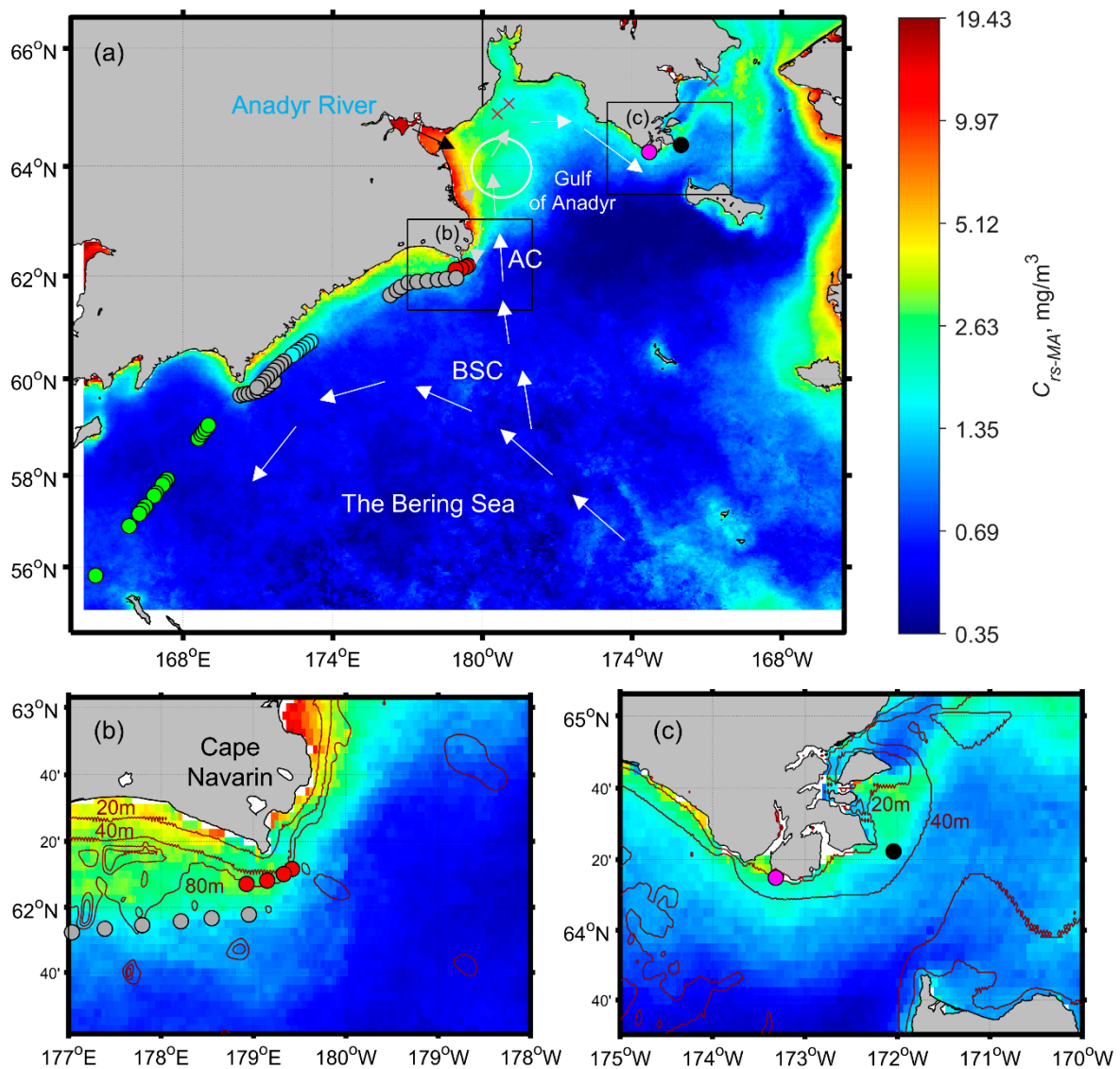


Figure 1. The study area is the western part of the Bering Sea in August 2013: (a) the entire study area; (b) the region near Cape Navarin; (c) the region near eastern part of the Gulf of Anadyr. BSC is the Bering Slope Current and AC is the Anadyr current. C_{rs-MA} is the averaged MODIS-Aqua estimations of chl-a for August in the period 2002–2020. A description of the colors of the dots is presented in Table 3.

Currently, there has not been a great deal of situ bio-optical and above-water remote sensing research in the Bering Sea carried out in the 21st century. However, the results obtained in the eastern part of the Bering Sea by Naik et al. [21,22] should be noted. In the works [23,24], the data represented the central and eastern parts of the Bering Sea. Salyuk et al. [25] presented results from the western part of the Bering Sea, where the retrieving accuracy for chl-a concentration was compared in MODIS-Aqua and VIIRS-SNPP satellite radiometers. In addition, it is necessary to mention the work of Hirawaki [26], where the features of the distribution of CDOM light absorption coefficients in the north-western part of the Bering Sea were considered.

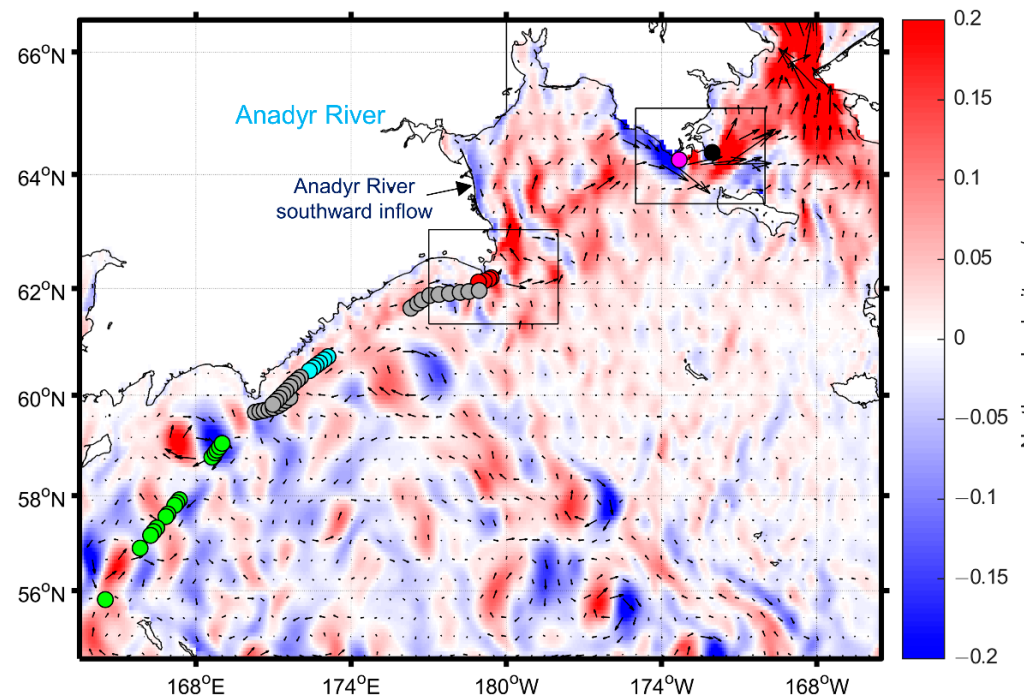


Figure 2. Northward velocity of the sea surface current averaged for the August 2013 (from the CMEMS reanalysis). A description of the colors of the dots is presented in Table 3.

The subarctic Bering Sea is the Pacific gateway through which the North Pacific and the Arctic Ocean exchange heat and water. The Pacific waters that are transited and modified across the wide Bering Sea shelf substantially affect the environmental state in the Arctic. Research in the Bering Sea is influenced by various hydrophysical processes. Upwelled deeper Pacific waters with relatively high salinity and nutrient content enter the Gulf of Anadyr (GA) with the Bering Slope Current (BSC), forming the Anadyr Current (AC), which flows clockwise along eastern Siberia to the Anadyr Strait and further into the Chukchi Sea [27–30]. The interaction between the AC and the Anadyr River outflow forms frontal sections and local eddies in the southern GA during the summer season [27]. There is also evidence of an episodic narrow coastal current of the Anadyr River waters that flows southward around Cape Navarin [28]. The freshwater runoff from the Anadyr River strongly influences the coast of the Gulf of Anadyr and can reach Cape Navarin [31–33]. These riverine waters are characterized by a high CDOM content [32–34]. It should be noted that the southward flow of riverine waters was observed during August 2013 (Figure 2).

3. Materials and Methods

In situ data were obtained using calibrated fluorescence measurements of chl-a concentration and CDOM content. The remote data included measurements from the MODIS-Aqua, MODIS-Terra, and VIIRS-SNPP satellite multispectral ocean color radiometers and shipborne above-water measurements obtained using an ASD hyperspectral radiometer. In addition, the simulated values of the CZCS, OCTS, OLCI, MERIS, MODIS, SeaWiFS, SGLI, and VIIRS multispectral satellite radiometers obtained by applying the corresponding spectral response functions to ship hyperspectral data were analyzed.

3.1. In Situ Measurements

In the present work, three approaches were carried out for the direct measurement of chl-a and CDOM; each of them are described below.

- (1) Most of the data were obtained via flow-through fluorometer measurements during the ship's entire route. The fluorometer provided hyperspectral measurements of seawater fluorescence induced by 355 nm and 532 nm laser radiation for CDOM

- (D_{flow}) and chl-a (C_{flow}) fluorescence intensity estimations, as described in [35,36]. This approach provided a significant quantity of synchronous remote sensing and in situ measurements during two passages through the Bering Sea. The corresponding spatial resolution was about 113 m for a ship speed equal to 11 knots. In addition, the temperature (T) and salinity (S) of seawater were measured in the flow-through system.
- (2) Submersible measurements were carried out to take into account the vertical distribution of chl-a and CDOM. A SeaBird SBE 19-plus v.1 profiler with the additional calibrated fluorescence sensors WETStar-chlA and WETStar-CDOM and a spherical photosynthetically available radiation (PAR) sensor Licor LI-193 were used to measure chl-a concentrations (C_{CTD}), CDOM content (D_{CTD}), and PAR values (PAR), respectively.
 - (3) Regular samplings of the seawater from the flow system at various depths were carried out for standard laboratory spectrophotometric analysis. These measurements allowed us to validate the in situ fluorometric estimations of chl-a, which could be affected not only by chl-a concentrations but also the composition and/or functional state of phytoplankton. The values for CDOM fluorescence were normalized to quinine sulfate concentrations (QSU units in mg/m^3) using standard laboratory calibration.

For each SBE 19-plus cast, vertical profiles were derived for calibrated chl-a concentrations and CDOM content. The “optically weighted” values [37] for chl-a concentration and CDOM content were calculated, taking into account the PAR [12,25]:

$$C_{CTD}^{ow} = \frac{\int_0^{z_{eu}} C_{CTD}^*(z)w(z)dz}{\int_0^{z_{eu}} w(z)dz}, \quad (1)$$

$$D_{CTD}^{ow} = \frac{\int_0^{z_{eu}} D_{CTD}^*(z)w(z)dz}{\int_0^{z_{eu}} w(z)dz}, \quad (2)$$

$$w(z) = PAR(z)^2, \quad (3)$$

where z is the depth value; z_{eu} is the euphotic depth, which is equal to the depth where 1% of surface PAR is measured; w is the optical weight calculated from the PAR measurements; C_{CTD}^* and D_{CTD}^* are the values corrected for the laboratory standard measurements.

Then, the flow-through measurements of chl-a and CDOM were calibrated for the “optically weighted” values of chl-a and CDOM and estimations of the in situ values for chl-a concentration (C_{ins}) and CDOM content (D_{ins}) were obtained as follows:

$$C_{ins} = 2.62 \times C_{flow}, R^2 = 0.8 \quad (4)$$

$$D_{ins} = 0.0272 \times D_{flow}, R^2 = 0.8 \quad (5)$$

where the proportionality factors were determined by the comparison of C_{flow} and D_{flow} with C_{CTD}^{ow} and D_{CTD}^{ow} , respectively, and R^2 is the coefficient of determination. The intercept value was not calculated since the R^2 value remained significant. In further analysis, the C_{ins} and D_{ins} values were used.

3.2. Hyperspectral Remote Sensing Above-Water Ocean Color Measurements

The hyperspectral remote sensing measurements of Rrs were carried out using an above-water ASD Fieldspec HandHeld (Analytical Spectral Devices Inc., Boulder, CO, USA) spectroradiometer (325–1100 nm; 1 nm spectral resolution; 10° field of view) from the ship. The usefulness of this instrument has successfully been proven in similar ocean color experiments [38]. The recordings were carried out with the sun zenith angle at less than 60 degrees for clear or completely cloudy skies. A total of 54 quality measurements were performed.

The experimental data obtained on board the ship have several advantages. First, the hyperspectral measurements of the upwelling radiation from the sea allow for the determination of the optimal spectral range for developing bio-optical algorithms. Second, atmospheric correction is not required, which eliminates inaccuracies associated with the passage of the recorded signal through the atmosphere. Thus, the remaining uncertainty is associated only with changes in the ratios between the different OACs or, in other words, with the choice of the correct bio-optical algorithm.

The R_{rs} spectrum ($R_{rs}(\lambda)$) is the fundamental apparent optical property of seawater used in bio-optical algorithms to retrieve the OAC content. The following formula can be used to define this parameter:

$$R_{rs}(\lambda) = \frac{L_w(\lambda)}{E_S(\lambda)}, \quad (6)$$

where $L_w(\lambda)$ is the water-leaving radiance in the zenith direction; E_S is downwelling incident irradiance measured above the sea surface; and λ is the central wavelength of the spectral channel.

The experimental determination of $R_{rs}(\lambda)$ above the surface was based on the method described in [39] (see “Method 2: Uncalibrated radiance and reflectance plaque measurements”):

$$R_{rs}(\lambda, \theta, \varphi) = \frac{L_w(\lambda, \theta, \varphi)}{E_S(\lambda)} = \frac{F_L(\lambda) [S_{srf}(\lambda, \theta, \varphi) - \rho S_{sky}(\lambda, \theta_{sky}, \varphi)]}{F_L(\lambda) \left[\frac{\pi S_g(\lambda, \theta_g, \varphi_g)}{R_g(\lambda, \theta_g, \varphi_g)} \right]}, \quad (7)$$

where θ is the sensor’s sea-viewing zenith angle; θ_{sky} is sky-viewing zenith angle; φ is the azimuth viewing angle relative to the sun azimuth; θ_g and φ_g are the viewing angles at the reflectance plaque; $L_w(\lambda, \theta, \varphi)$ is the water-leaving radiance in the θ, φ direction; $F_L(\lambda)$ is the instrument’s unknown radiance response calibration factor, which will be eliminated after division; S_{srf} is the uncalibrated sea surface radiance; S_{sky} is the uncalibrated sky radiance, measured in the direction of the specular reflection of sky radiance; ρ is the sea surface reflectance coefficient, which is a function of the viewing and sun direction and sea surface wave conditions; and S_g is the uncalibrated reflected radiance from the reflectance plaque corrected for the known bi-directional reflectance function R_g (BRDF).

The coefficient ρ was calculated following the procedure described in [40,41], which parameterizes the reflectance as a function of solar direction and near-surface wind velocity. The ρ values were in the range of 0.025–0.031.

Spectralon[®], with a 99% reflectance value, was used in this work as the reflectance plaque. The R_g values were verified using an Agilent Cary spectrophotometer with a fiber-optic attachment before and after the expedition.

In each of the experiments conducted to determine $R_{rs}(\lambda, \theta, \varphi)$ the following procedure was performed. A total of 20–25 sea surface radiation spectra S_{srf} , 30 sky radiation spectra S_{sky} , and 50 reflectance plaque radiation spectra S_g were sequentially measured for the recommended θ and φ angles: 40° absolute and 135° related to the sun’s direction, respectively. A handheld working scheme was used to improve the compensation for vessel pitching. Furthermore, for this purpose, a median spectrum was selected from each series for further analysis. In addition, continuous measurements of above-water downwelling PAR were carried out using two Licor Li-192 sensors; the obtained data were used to remove the $R_{rs}(\lambda, \theta, \varphi)$ spectrum from further consideration in the case of abrupt changes in ambient light conditions.

The obtained $R_{rs}(\lambda, \theta, \varphi)$ spectra were not directly comparable with the satellite-derived $R_{rs}(\lambda)$. Thus, we used SeaDAS version 7 code and lookup tables for the BRDF correction procedure (based on NASA Ocean Optics Protocols [42]) in order to compare the above-water measurements with satellite data and to potentially apply standard ocean color algorithms for shipboard data. For more details on these procedures, see also [43].

3.3. Multispectral Remote Sensing Satellite Ocean Color Measurements

For the analysis, data from the second level of satellite radiometers—MODIS/Aqua, MODIS/Terra, and VIIRS/Suomi-NPP—processed according to Reprocessing 2018.0 were used. A comparison with ship measurements was carried out by searching for satellite data in the time interval ± 6 h and ± 4 km from the ship data point, according to [25]. Further, in the obtained sample of satellite pixels, outliers were filtered using the 3-sigma criterion and the average $R_{rs}(\lambda)$ values were calculated at all available wavelengths in the visible range.

3.4. Simulated Data of Multispectral Satellite Radiometers

The spectral response functions (srf) for global one-day and two-day spatial coverage satellite radiometers were used to determine regional bio-optical algorithms. The srf data were downloaded from [44].

Table 1 lists the names of the analyzed satellite radiometers and their spectral bands available between 375 and 575 nm. Each cell of Table 1 contains the central wavelength of the spectral response function between the edges at half-height (λ_{center}) and the value of the full width at half maximum (FWHM). The values are presented in the following form: " $\lambda_{center}/FWHM$ ". The b1, b2, . . . , and b7 are notations for the considered spectral ranges.

Table 1. Spectral bands in the 374–576 nm range available on analyzed satellite radiometers. Each cell contains information structured as λ_{center} (nm)/FWHM (nm).

Radiometer/Satellite	Sat ID	Spectral Bands (in nm)						
		b1	b2	b3	b4	b5	b6	b7
		374–403	404–424	431–454	456–475	476–500	501–539	540–576
CZCS/Nimbus-7	CN	–	–	442.6/22.2	–	–	520.5/20.8	550.6/20.1
OCTS/ADEOS	CA	–	412.4/17.5	442.9/19.9	–	490.2/22.8	516.4/14.7	565.1/19.2
OLCI/Sentinel-3A	OA	399.9/14.0	411.9/9.8	443.0/9.9	–	490.5/10.0	510.4/10.0	560.4/10.0
OLCI/Sentinel-3B	OB	400.3/13.3	411.9/9.9	443.0/9.9	–	490.4/10.0	510.4/10.0	560.4/10.0
MERIS/EnviSat	ME	–	412.5/9.9	442.5/9.9	–	490.0/10.0	510.0/10.0	560.0/10.0
MODIS/Aqua, 1000 m	MA	–	412.1/14.5	442.3/9.7	–	487.5/10.7	530.2/12.0	547.4/10.4
MODIS/Terra, 1000 m	MT	–	411.6/14.7	442.2/9.7	–	487.1/10.6	529.8/12.0	547.0/10.3
MODIS/Aqua, 500 m	MA-HI	–	–	–	466.1/18.9	–	–	554.0/19.8
MODIS/Terra, 500 m	MT-HI	–	–	–	466.1/18.9	–	–	554.0/19.8
SeaWiFS/OrbView-2	SO	–	413.3/20.1	443.9/19.6	–	491.1/20.6	510.1/22.4	554.6/18.3
SGLI/GCOM-C	SG	379.8/10.6	412.4/10.4	443.2/10.1	–	489.8/10.3	529.5/19.1	566.1/19.8
VIIRS/Suomi-NPP	VS	–	410.5/20.5	443.1/15.2	–	486.2/19.3	–	550.7/19.8
VIIRS/JPSS-1	VJ	–	410.9/18.2	444.8/17.1	–	488.7/19.1	–	556.5/18.1

3.5. Obtained Experimental Dataset

Using the methods described above, an experimental data array was obtained and used for the analysis, the summary of which is presented in Table 2. To determine the quality of the atmospheric correction of satellite data for different spectral channels, the data for shipborne and available satellite measurements of R_{rs} were compared. The shipboard surface hyperspectral data and simulated data for the satellite multispectral radiometers were used to develop regional bio-optical algorithms.

Table 2. The number of points in each type of data used.

In Situ Measurements	Shipborne Remote Sensing Hyperspectral Measurements	Satellite Multispectral Remote Sensing Measurements			Simulated Multispectral Values
		MA	MT	VS	
54	54	47	48	48	54

Although the total number of points was not large, a wide range of chl-a concentrations from 0.17 to 9.29 mg/m³ uniformly filled in the array. In addition, for most points, there were synchronous in situ and satellite measurements; thus, the results obtained could be used to build bio-optical algorithms.

3.6. Considered Empirical Bio-Optical Algorithms

The following equations were used as the tested OCx-like (Ocean Color) bio-optical algorithms for estimating the concentration of chl-a (C_{rs}) and CDOM content (D_{rs}) from the remote sensing data [45]:

$$C_{rs}(\lambda_C) = 10^{(c_0 + c_1 * \log_{10}(R_{OCx}))}, \quad (8)$$

$$D_{rs}(\lambda_D) = 10^{(d_0 + d_1 * \log_{10}(R_{OC2}(\lambda_D)))}, \quad (9)$$

$$R_{OC2}(\lambda) = \frac{R_{rs}(\lambda)}{R_{rs}(\lambda_{b7})}, \quad (10)$$

$$R_{OC3} = \frac{\max(R_{rs}(\lambda_{b3}), R_{rs}(\lambda_{b5}))}{R_{rs}(\lambda_{b7})}, \quad (11)$$

$$R_{OC3}^* = \frac{\max(R_{rs}(\lambda_{b3}), R_{rs}(\lambda_{b6}))}{R_{rs}(\lambda_{b7})}, \quad (12)$$

$$R_{OC4} = \frac{\max(R_{rs}(\lambda_{b3}), R_{rs}(\lambda_{b5}), R_{rs}(\lambda_{b6}))}{R_{rs}(\lambda_{b7})}, \quad (13)$$

where R_{OCx} is the band ratio index determined by Formulas (10), (11), (12), or (13); R_{OC3}^* is used for the CZCS radiometer; λ_C and λ_D are the wavelengths for estimating the concentration of chl-a and CDOM content, respectively, in the case of R_{OC2} ; λ_{bi} is the wavelength from i -th spectral range; λ_{b7} is the wavelength from the b7 spectral range used for normalization in the band ratio index for the ASD hyperspectral radiometer ($\lambda_{b7} = 555$); and c_i and d_i are the empirical coefficients.

To select optimal λ_C and λ_D values, it is necessary to use the spectral range determined by considering the OACs. The normalization wavelength λ_{b7} was selected to minimize the influence of all OACs except water.

In Formulas (8) and (9), only the first degree of the polynomial was used, since the array of points was not large enough to make a stable bio-optical algorithm with a large polynomial degree.

The list presented in [46] was used as a test set of global satellite bio-optical algorithms. The coefficients were derived using version 2 of the NASA bio-Optical Marine Algorithm Dataset (NOMAD).

3.7. Statistical Metrics

To determine the quality characteristics of the atmospheric correction, the mean relative absolute error (MRAE, in percent) was used, as described in [43]:

$$MRAE = 100 \frac{1}{N} \sum_{i=1}^N \frac{|y_{rs}(i) - y_{is}(i)|}{y_{is}(i)}, \quad (14)$$

where N is the number of samples, i is the index in the data array, $y_{rs}(i)$ are the remote sensing measurements, and $y_{is}(i)$ are the in situ measurements used as references.

Logarithmically transformed mean absolute differences (MAEL) and bias (BiasL), as recommended in [47], and the standard metric R-squared (R^2L) were used to determine the best spectral ranges for estimating the OAC content from remote sensing data and the quality of the work of the regional bio-optical algorithms:

$$MAEL = 10^{\left(\frac{1}{N} \sum_{i=1}^N |\log_{10}(y_{rs}^*(i)) - \log_{10}(y_{is}(i))| \right)}, \quad (15)$$

$$biasL = 10 \left(\frac{1}{N} \sum_{i=1}^N (\log_{10}(y_{rs}^*(i)) - \log_{10}(y_{is}(i))) \right), \quad (16)$$

$$R2L = 1 - \frac{\sqrt{\sum_{i=1}^N (\log_{10}(y_{is}(i)) - \log_{10}(y_{rs}^*(i)))^2}}{\sqrt{\sum_{i=1}^N (\log_{10}(y_{is}(i)) - \log_{10}(\bar{y}_{is}))^2}}, \quad (17)$$

where $y_{rs}^*(i)$ is the estimated OAC content from the remote sensing measurements calculated using Formula (8) or (9) or by global OCx algorithms. The same metrics were used in [18]. Here, the compared values were log-transformed since in this case, the distributions of the considered values were closer to a normal or near-normal distribution.

$BiasL$ was used for comparison only with the global bio-optical algorithms since in the case of calculating the regional algorithm, $BiasL$ will always be equal to 1 due to the use of the least squares method.

The obtained values of $BiasL$ and $MAEL$ can be interpreted as follows: a $BiasL$ value of 1.2 indicates that the model is $1.2 \times (20\%)$ greater on average than the observed variable; $MAEL$ always exceeds unity, such that an $MAEL$ of 1.5 indicates a relative measurement error of 50% [47].

For each calculated metric, a confidence interval with a 95% significance level was determined using the bootstrap method with the bias-corrected percentile procedure [48] and 2000 simulations. The Matlab function `bootci` was used for this purpose. This technique is very convenient in cases with small samples or a lack of information about the type of distribution of the analyzed values. The use of the bootstrap method for ocean color data was also performed in [49,50].

A test of the statistical hypothesis of a significant difference in the means between the samples obtained from the bootstrap simulations was also determined using the bootstrap method. For a difference between the two sample means to be considered significant, its 95% confidence intervals must not include zero. This approach was verified via a comparison with the results of a two-sample t -test (`ttest2` function in Matlab). In the case of testing the hypothesis for two normal distributions, the results of `ttest2` and the bootstrap approach almost completely coincided.

4. Results

4.1. Comparison of the Satellite and Shipborne Above-Water Remote Sensing Measurements

Figure 3 shows the spectral distribution of $MRAE$ for available data from the three satellite radiometers and the shipboard above-water measurements of R_{OC2} . It can be seen that in all three cases, high error was observed in the satellite R_{OC2} measurements in the spectral region of less than 440 nm, which is typical for the application of the atmospheric correction algorithm for satellite data [11,51].

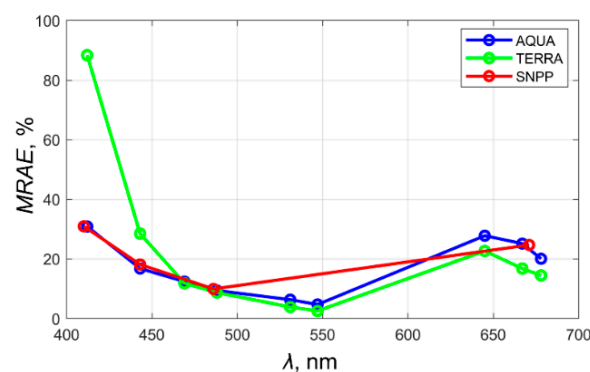


Figure 3. Quality analysis of the atmosphere correction of satellite data. Spectral distribution of $MRAE$ of the determination of satellite band ratio index $R_{OC2}(\lambda)$ relative to reference ship-based measurements.

Figure 4 shows examples of comparisons between R_{OC2} determined from satellite measurements and values obtained from shipborne surface measurements. It can also be seen that the *MRAE* was significantly higher in the 412 nm spectral band than in the 488 nm band.

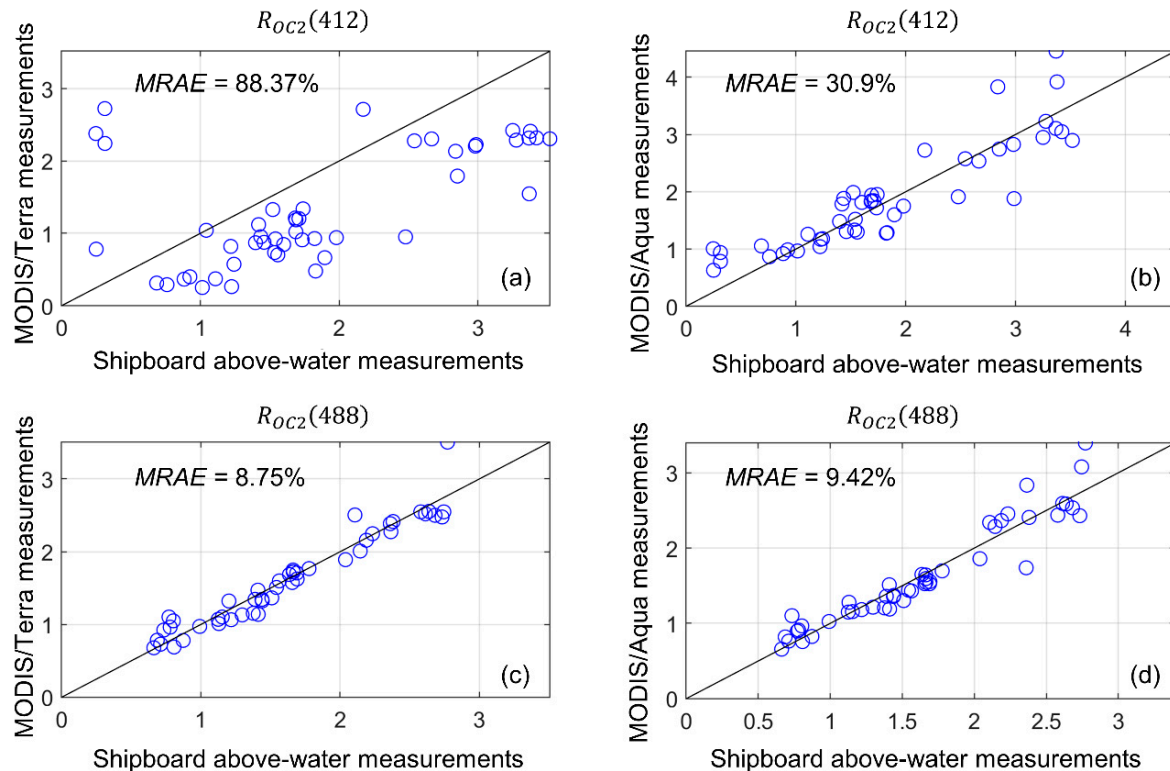


Figure 4. Quality analysis of the atmosphere correction of satellite data. Examples of the comparison of ship and satellite estimations of R_{OC2} . Left column shows MODIS/Terra measurements (a,c), right column shows MODIS/Aqua measurements (b,d).

To focus only on the development of bio-optical algorithms, shipborne surface R_{OCx} data were used for further analysis.

4.2. Comparison of Bio-Optical and Hydrophysical Parameters and Dataset Classification

Figure 5a shows the obtained spectra of $R_{rs}(\lambda)$ in the Bering Sea and scatterplots (Figure 5b–d) with different combinations of bio-optical and hydrophysical parameters.

The data are marked with the following colors: green denotes the southwestern part of the sea with low concentrations of chl-a and low CDOM content; grey represents the central part of the western side of the sea with medium CDOM content and medium concentrations of chl-a; cyan also denotes in the central part of the western side, but with high chl-a and medium CDOM; red is the southern part of Anadyr Bay with very high CDOM content and low salinity; magenta represents the northern part of Anadyr Bay with high CDOM content and low salinity, similar to the red dots but in a different geo-location; black denotes the northwestern part of the sea, similar to the gray points but with a lower seawater temperature because of its more northern geo-location. A summary of the selected water types is presented in Table 3.

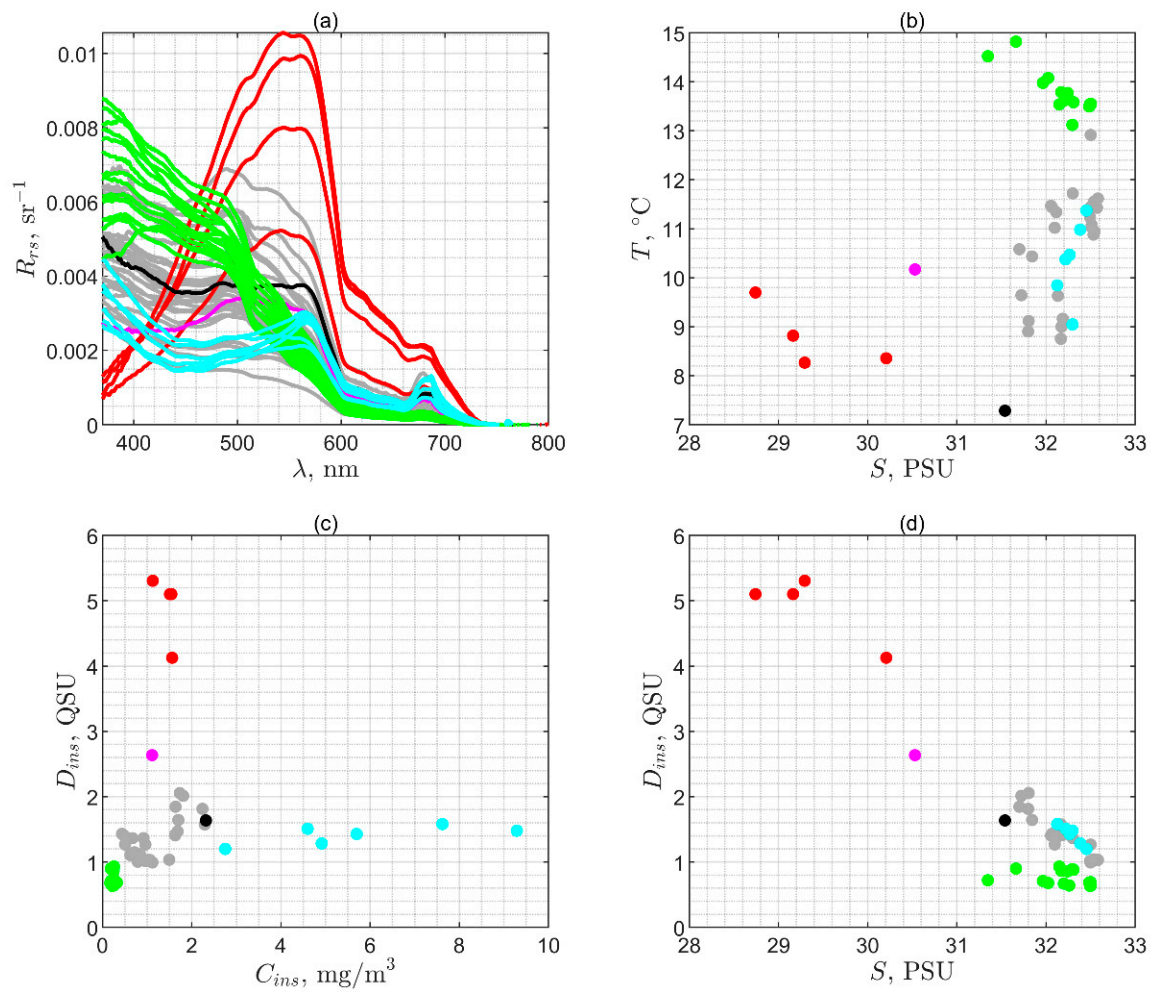


Figure 5. Remote sensing and in situ measurements of bio-optical and hydrophysical parameters in the Bering Sea: (a) spectral remote sensed reflectance measured above the water; (b) scatterplot of flow-through measurements of seawater temperature and salinity in Practical Salinity Units (PSU); (c) scatterplot of flow-through measurements of “optically weighted” chl-a concentration and CDOM content; (d) scatterplot of flow-through measurements of “optically weighed” CDOM content and seawater salinity.

Table 3. Summary of the selected water types.

Color	Location in the Bering Sea	Num. of Points	Characteristics	Time Periods
Green	Southwestern part of the sea	15	Low chl-a and low CDOM	3, 4, 28 August 2013
Grey	Central part of the western side of the sea	27	Medium chl-a and medium CDOM	4, 5, 27 August 2013
Black	Northwestern part of the sea	1	Similar to gray but with lower seawater temperature	7 August 2013
Cyan	Central part of the western side of the sea	6	Similar to gray but with high chl-a and medium CDOM	27 August 2013
Red	Southern part of Anadyr Bay	4	Medium chl-a and very high CDOM, low salinity	26 August 2013
Magenta	Northern part of Anadyr Bay	1	Similar to red but with lower CDOM and higher salinity	6 August 2013

4.3. Spectral Bands for the Optimal Determination of CDOM Content Using Remote Sensing

Figure 6 shows the spectral dependence of the calculated statistical metrics $R2L$ and $MAEL$ for comparing in situ CDOM content (D_{ins}) and the remote determination of D_{rs} , performed for different wavelengths λ_D according to Formulas (9) and (10), using ASD hyperspectral data.

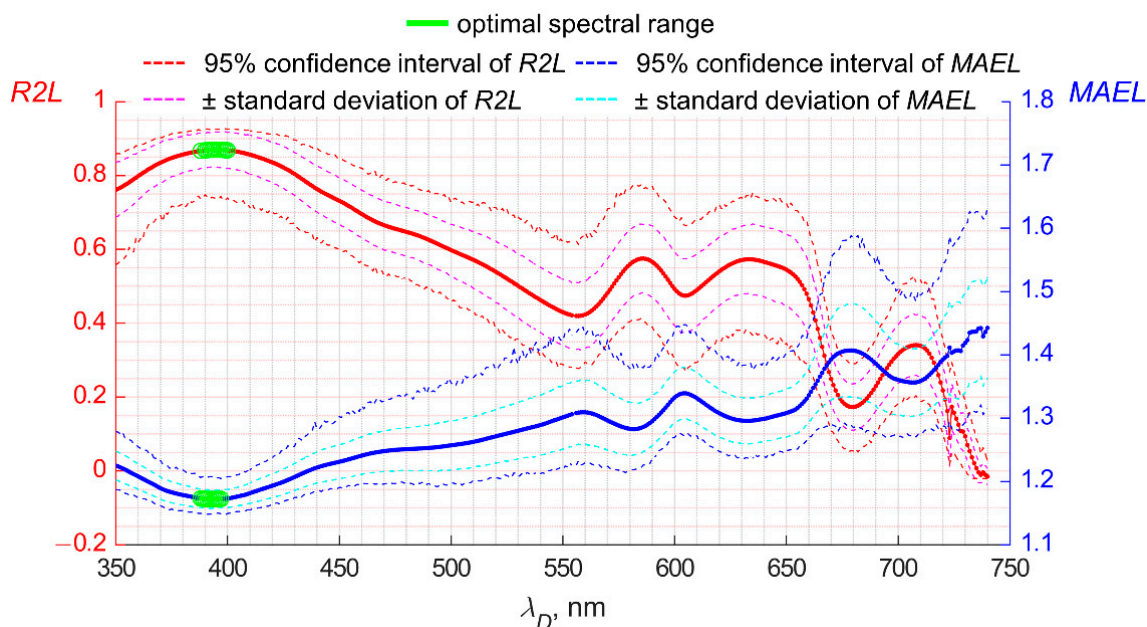


Figure 6. Spectral distribution of $R2L$ and $MAEL$ for the comparison of D_{ins} and D_{rs} calculated using Formula (9) from ASD hyperspectral data using $R_{OC2}(\lambda_D)$ band ratio indices.

The green color marks the range with the lowest $MAEL$ and statically insignificant changes in the best $MAEL$ value, which was equal to 388–397 nm. A similar calculation for the spectral distribution of $R2L$ gave a value for the optimal spectral range from 388 to 400 nm. Thus, the combined spectral range is equal to 388–397 nm.

Figure 7 shows scatterplots of the logarithms of in situ chl-a concentration or CDOM content versus R_{OC2} band ratio index for the first three spectral ranges considered— $b1$, $b2$, and $b3$ —which should be better for determining CDOM. The data for chl-a are presented here for comparison such that the change in the quality of the approximation for both considered OACs can be clearly observed. All plots are shown using the OLCI/S3A spectral response functions as an example because this type of radiometer has the full set of analyzed bands. For other radiometers, the results will be mostly similar, differing only in minor details.

Similar calculations were performed for all considered satellite radiometers and spectral bands from Table 1. The results for $R2L$ are shown in Table 4 and for $MAEL$ in Table 5. The best results are highlighted in green and mediocre results are in yellow.

4.4. Spectral Bands for the Optimal Determination of Chl-a Concentration Using Remote Sensing

Similar calculations were performed to determine the best spectral characteristics and optimal band ratio indices for estimating chl-a concentration.

Figure 8 shows the spectral distribution of the statistical metrics under consideration, where the optimal spectral ranges are marked in green. According to $R2L$, the optimal spectral range is from 521 nm to 536 nm, while according to $MAEL$, it is from 504 nm to 530 nm. The combined spectral range is 521–530 nm.

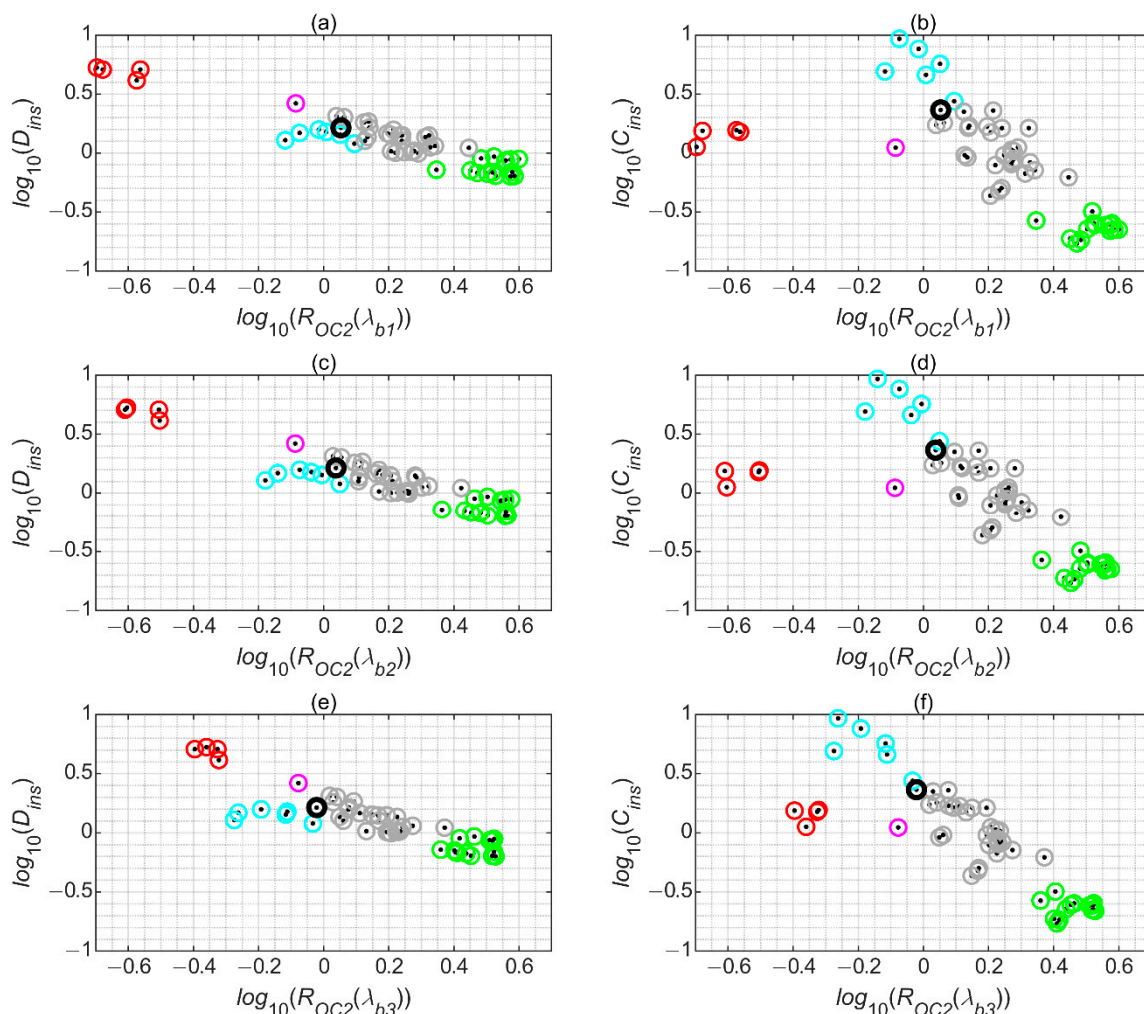


Figure 7. Scatterplots of the logarithms of in situ CDOM content (D_{ins}) (a,c,e) or chl-a concentrations (C_{ins}) (b,d,f) versus R_{OC2} band ratio index for the first three spectral ranges considered: b1 (a,b), b2 (c,d), and b3 (e,f). Band ratio values were obtained by applying OLCI/S3A spectral response functions to shipborne hyperspectral measurements collected using an ASD radiometer.

Table 4. R2L values for comparison between measured in situ CDOM content (D_{ins}) and estimated remote sensed CDOM content (D_{rs}) calculated using Formula (9) for spectral bands from b1 to b6. Columns with the best results are highlighted in green, and columns with mediocre, but acceptable results are highlighted in yellow.

Sat ID	$R_{OC2}(\lambda_{b1})$	$R_{OC2}(\lambda_{b2})$	$R_{OC2}(\lambda_{b3})$	$R_{OC2}(\lambda_{b4})$	$R_{OC2}(\lambda_{b5})$	$R_{OC2}(\lambda_{b6})$
CN	—	—	0.77	—	—	0.57
CA	—	0.84	0.74	—	0.62	0.55
OA	0.87	0.85	0.74	—	0.62	0.56
OB	0.87	0.85	0.74	—	0.62	0.56
ME	—	0.85	0.75	—	0.62	0.57
MA	—	0.86	0.78	—	0.66	0.54
MT	—	0.87	0.78	—	0.66	0.55
MA-HI	—	—	—	0.69	—	—
MT-HI	—	—	—	0.69	—	—
SO	—	0.85	0.75	—	0.63	0.58
SG	0.86	0.84	0.74	—	0.62	0.51
VS	—	0.86	0.77	—	0.65	—
VJ	—	0.86	0.75	—	0.63	—

Table 5. MAEL values for comparison between measured in situ CDOM content (D_{ins}) and estimated remote sensed CDOM content (D_{rs}) calculated using Formula (9) for spectral bands from b1 to b6. Columns with the best results are highlighted in green, and columns with mediocre, but acceptable results are highlighted in yellow.

ID Sat	$ROC_2(\lambda_{b1})$	$ROC_2(\lambda_{b2})$	$ROC_2(\lambda_{b3})$	$ROC_2(\lambda_{b4})$	$ROC_2(\lambda_{b5})$	$ROC_2(\lambda_{b6})$
CN	—	—	1.22	—	—	1.27
CA	—	1.19	1.23	—	1.26	1.27
OA	1.18	1.19	1.23	—	1.26	1.27
OB	1.18	1.19	1.23	—	1.26	1.27
ME	—	1.19	1.23	—	1.26	1.27
MA	—	1.18	1.22	—	1.25	1.27
MT	—	1.18	1.22	—	1.25	1.27
MA-HI	—	—	—	1.24	—	—
MT-HI	—	—	—	1.24	—	—
SO	—	1.19	1.23	—	1.25	1.26
SG	1.18	1.19	1.23	—	1.26	1.28
VS	—	1.18	1.22	—	1.25	—
VJ	—	1.18	1.23	—	1.25	—

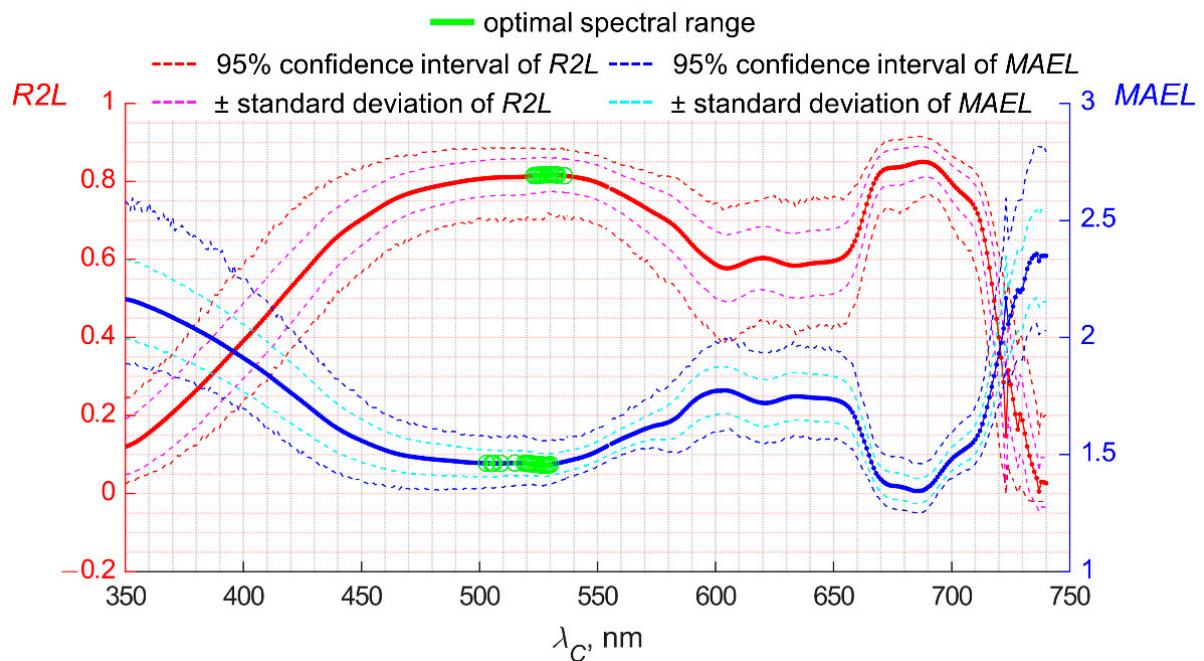


Figure 8. Spectral distribution of $R2L$ and $MAEL$ for the comparison of C_{ins} and C_{rs} calculated using Formula (8) from ASD hyperspectral data using $ROC_2(\lambda_C)$ band ratio indices.

Figure 9 shows scatterplots of the logarithms of the chl-a concentration or CDOM content versus the OC2 band ratio indices for the fifth and sixth spectral ranges and the OC3 and OC4 band ratio indices, which should be better for determining the chl-a concentration.

Tables 6 and 7 compare the considered statistical metrics for determining the chl-a concentration for different band ratio indices and various spectral response function characteristics.

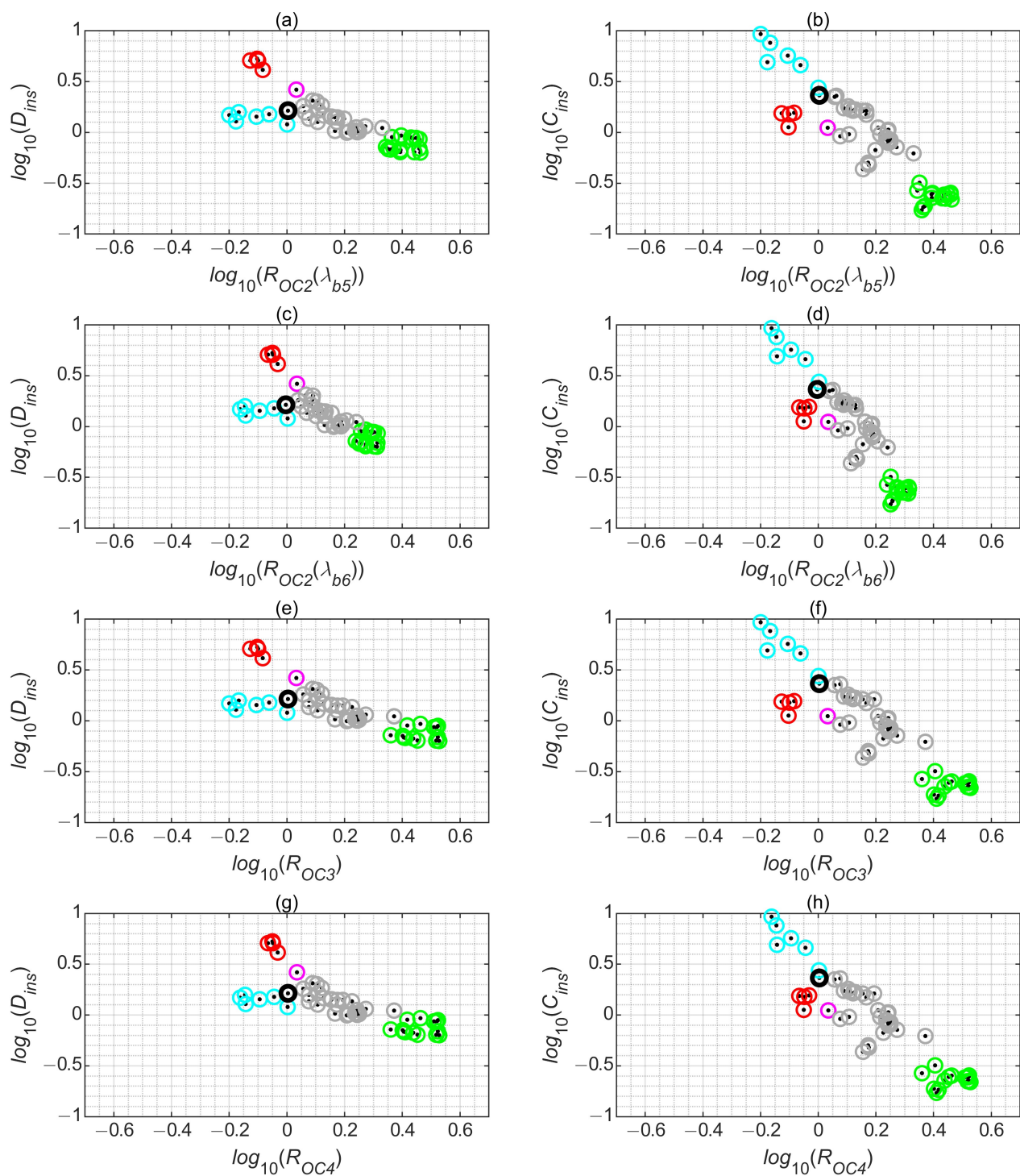


Figure 9. Scatterplots of the logarithms of in situ CDOM content (D_{ins}) (a,c,e,g) or chl-a concentrations (C_{ins}) (b,d,f,h) versus R_{OC2} band ratio index for the b5 (a,b) and b6 (c,d) spectral ranges and versus R_{OC3} (e,f) and R_{OC4} (g,h). Band ratio values were obtained by applying OLCI/S3A spectral response functions to shipborne hyperspectral measurements collected using an ASD radiometer.

Table 6. *R*_{2L} values for comparison between measured in situ chl-a concentration (C_{ins}) and estimated remote sensed chl-a concentrations (C_{rs}) calculated using Formula (8) for different band ratio indices. Columns with the best results are highlighted in green, and columns with mediocre, but acceptable results are highlighted in yellow.

ID Sat	$R_{OC>2}(\lambda_{b>1})$	$R_{OC>2}(\lambda_{b>2})$	$R_{OC>2}(\lambda_{b>3})$	$R_{OC>2}(\lambda_{b>4})$	$R_{OC>2}(\lambda_{b>5})$	$R_{OC>2}(\lambda_{b>6})$	$R_{OC>3}$	$R_{OC>4}$
CN	—	—	0.66	—	—	0.82	0.82 *	—
CA	—	0.52	0.7	—	0.8	0.81	0.82	0.83
OA	0.43	0.5	0.69	—	0.81	0.81	0.82	0.83
OB	0.43	0.5	0.69	—	0.81	0.81	0.82	0.83
ME	—	0.51	0.69	—	0.81	0.81	0.81	0.83
MA	—	0.46	0.65	—	0.78	0.82	0.79	0.81
MT	—	0.44	0.65	—	0.78	0.82	0.79	0.81
MA-HI	—	—	—	0.76	—	—	—	—
MT-HI	—	—	—	0.76	—	—	—	—
SO	—	0.49	0.69	—	0.8	0.81	0.81	0.83
SG	0.32	0.52	0.7	—	0.8	0.8	0.81	0.84
VS	—	0.45	0.67	—	0.79	—	0.8	—
VJ	—	0.48	0.69	—	0.8	—	0.81	—

* Formula (12) was used for R_{OC3} calculation.

Table 7. *MAEL* values for comparison between measured in situ chl-a concentrations (C_{ins}) and estimated remote sensed chl-a concentrations (C_{rs}) calculated using Formula (8) for different band ratios. Columns with the best results are highlighted in green, and columns with mediocre, but acceptable results are highlighted in yellow.

ID Sat	$R_{OC2}(\lambda_{b1})$	$R_{OC2}(\lambda_{b2})$	$R_{OC2}(\lambda_{b3})$	$R_{OC2}(\lambda_{b4})$	$R_{OC2}(\lambda_{b5})$	$R_{OC2}(\lambda_{b6})$	R_{OC3}	R_{OC4}
CN	—	—	1.62	—	—	1.46	1.41 *	—
CA	—	1.79	1.58	—	1.47	1.47	1.44	1.41
OA	1.89	1.81	1.58	—	1.47	1.46	1.44	1.42
OB	1.89	1.81	1.58	—	1.47	1.46	1.44	1.42
ME	—	1.8	1.59	—	1.47	1.46	1.44	1.42
MA	—	1.85	1.62	—	1.49	1.45	1.47	1.43
MT	—	1.86	1.62	—	1.49	1.45	1.47	1.43
MA-HI	—	—	—	1.5	—	—	—	—
MT-HI	—	—	—	1.5	—	—	—	—
SO	—	1.82	1.58	—	1.47	1.46	1.45	1.42
SG	2.01	1.79	1.58	—	1.47	1.49	1.44	1.41
VS	—	1.87	1.61	—	1.48	—	1.46	—
VJ	—	1.83	1.58	—	1.47	—	1.45	—

* Formula (12) was used for R_{OC3} calculation.

The in situ measurements of chl-a concentration (C_{ins}) were also compared with the algorithm-derived estimations of chl-a C_{rs} by the global bio-optical algorithms presented at https://oceancolor.gsfc.nasa.gov/atbd/chlor_a/ (accessed on 15 November 2022). The calculated metrics are shown in Table 8. The result obtained gives an idea of the applicability of global bio-optical algorithms.

Table 8. Quality of applying the global bio-optical algorithms presented at https://oceancolor.gsfc.nasa.gov/atbd/chlor_a/ (accessed on 15 November 2022) to an estimation of chl-a concentration from shipboard remote sensed hyperspectral data by applying the corresponding spectral response function (srf). Statistical metrics were calculated by the comparison of in situ chl-a measurements (C_{ins}) and remote sensed estimations C_{rs} . The best results are highlighted in green, mediocre in yellow, and worst in orange.

Global Bio-Optical Algorithm	Default Satellite Sensor	Applied srf	MAEL	BiasL	R2L
OC4	SeaWiFS	SO	1.44	1.05	0.82
OC4E	MERIS	ME	1.45	1.05	0.82
OC4O	OCTS	CA	1.5	1.2	0.79
OC3S	SeaWiFS	SO	1.49	1.07	0.79
OC3M	MODIS	MA	1.5	1.05	0.77
OC3M	MODIS	MT	1.51	1.04	0.77
OC3V	VIIRS	VS	1.51	1.08	0.77
OC3V	VIIRS	VJ	1.54	1.18	0.77
OC3E	MERIS	ME	1.49	1.07	0.79
OC3O	OCTS	CA	1.54	1.19	0.76
OC3C	CZCS	CN *	1.46	1.09	0.81
OC2S	SeaWiFS	SO	1.53	0.97	0.78
OC2E	MERIS	ME	1.52	0.99	0.78
OC2O	OCTS	CA	1.56	1.1	0.76
OC2M	MODIS	MA	1.51	0.98	0.77
OC2M	MODIS	MT	1.51	0.98	0.77
OC2M-HI	MODIS, 500 m	MA	1.66	1.01	0.68
OC2M-HI	MODIS, 500 m	MT	1.66	1	0.68

* Formula (12) was used for R_{OC3} calculation.

5. Discussion

The presented results are consistent with the general concepts of the spectral absorption ranges of phytoplankton and CDOM in seawater. In the spectral range $\lambda_C = 490 \dots 540$ nm (Figure 8), the influence of light absorption by phytoplankton cells increased compared to CDOM; to the contrary, in the range $\lambda_D = 350 \dots 430$ nm (Figure 6), the relative contribution of CDOM became greater. Thus, these are the best spectral ranges for determining the chl-a concentration and CDOM content, respectively (spectral range I).

In addition, we identified the mediocre spectral range II, which included low MAEL values at $\lambda_C = 490 \dots 540$ (Figure 8) and $\lambda_D = 570 \dots 650$ nm (Figure 6). In this case, the relationship between D_{rs} and D_{ins} became positively proportional. This could be due to the significant contribution of CDOM fluorescence to the R_{rs} spectrum at high CDOM concentrations or to the possible natural covariation of CDOM and suspended particles [52].

In addition, we identified two spectral ranges III and IV with low MAEL values associated with the solar-induced fluorescence of chl-a when C_{rs} was estimated at $\lambda_C = 670 \dots 710$ (Figure 8) and $\lambda_D = 350 \dots 430$ nm or $\lambda_D = 570 \dots 650$ nm (Figure 6). The peak near 680 nm represents sun-induced fluorescence FLH, which depends on the chl-a concentration, functional state and species composition of phytoplankton, etc. [53]. FLH could be retrieved from MODIS data using three spectral bands: 680 nm for FLH intensity and bands near 660 and 750 nm for background signal estimation [54].

Statistically, the best spectral range for determining CDOM content includes wavelengths from 388 to 397 nm, while that for the determination of chl-a concentration contains wavelengths from 521 to 530 nm (Figures 6 and 8). It is in these ranges that sufficient measurement accuracy is maintained with the least influence of the considered OACs on each other.

A comparison of the multispectral characteristics of radiometers (Tables 4–7) showed that their differences arise mainly from changes in the spectral range used, and not from a variation in the spectral characteristics of individual radiometers in the same spectral ranges. At the same time, the spectral response functions of scanners from the same family are slightly different from each other, which may lead to differences in the obtained results [55].

However, in the available dataset, the existing small spectral differences between similar radiometers did not lead to significant differences in the obtained results, except in the case of VIIRS-family radiometers.

When analyzing data, it is necessary to keep in mind that the use of spectral bands around 400 and 412 nm in measurements from space has significant disadvantages associated with the maximum error of atmospheric correction, especially in the presence of absorbing aerosols. In addition, the complexity of taking into account the influence of sea waves on the reflectivity of the sea surface in UV and blue diapason should be considered [51,56,57]. This was also confirmed by our results, presented in Figures 3 and 4. Given this, it is necessary to develop new methods for atmospheric correction that use bands ≤ 400 nm to improve the measurement of water-leaving radiance at 412 nm or a more strict approach to filtering data with complex atmospheric conditions or wave characteristics [58,59].

5.1. CDOM Content Determination

The presence of red and magenta dots (Table 3 and Figure 5) represents the main contribution to the spectral distribution of the statistical metrics following the theoretical concepts of CDOM absorption. When comparing R_{OC2} with D_{ins} , these points lie on a straight line for the b1, b2 and b3 spectral range, while for chl-a, these points fall out of the linear dependence (Figure 7).

It can be seen from the red and magenta dots that an increased content of CDOM was observed relative to the expected content, which might be explained by the functional status of the phytoplankton cells (Figure 5c). This additional CDOM content is most likely associated with the influence of river flows, which was confirmed by the lower salinity, as shown in Figure 5b. At the same time, an inverse significant relationship can be observed on the scatter plot " D_{ins} -S" for both the red and magenta and the black and grey points, which may also indicate the influence of terrigenous waters. This could be the impact of both local rivers and the waters of the Anadyr River, whose flow is about 60 km³ a year [32,33].

In general, the CDOM determination results from the b2 spectral range were not considerably worse than those from the b1 range (Tables 4 and 5); therefore, they can also be used to estimate CDOM, and the b1 range can be used for new atmospheric correction algorithms [60].

In addition, the b3 range can be used to estimate the CDOM, as, for example, was carried out in the work of Kopelevich [11]. However, in this case, it is necessary to be careful, since the strong influence of phytoplankton absorption begins to affect the estimation. The $R2L$ values were improved when comparing R_{OC2} with CDOM content versus with chl-a concentration (compare Tables 4 and 6 for the b3 spectral range). The algorithm for determining CDOM content from the b3 spectral range can be used to estimate the order of magnitude or to assess the quality of the atmospheric correction by comparison with the b2 channel, but not to determine the true CDOM fields independent of chl-a.

Determining the CDOM from the spectral range $\lambda_D = 570 \dots 650$ nm is not yet recommended. Firstly, there are no suitable satellite channels in multispectral instruments. Secondly, the statistical relationship is not very strong, and thirdly, it is most likely associated not only with direct, but also with indirect natural factors.

5.2. Chl-a Concentration Determination

The presence of cyan dots, in which the relative content of chl-a was higher than for dots of other types (Table 3 and Figure 5), showed an increase in the error of the results from the determination of CDOM content in a wavelength range of b3, b4, b5 or b6 (Figures 7 and 9). At the same time, in the same spectral ranges these points were well-described by a single straight line when comparing R_{OCx} and C_{ins} (Figures 7 and 9).

The optimal results for the determination of chl-a concentration were provided by the multi-wavelength OC3-like and OC4-like algorithms (Tables 5 and 6) and were in agreement with the results of the global bio-optical algorithms [18]. At the same time, algorithms from the OC2 family for channels from the b5 and b6 bands also provided

reasonable results and can be used in the case of large atmospheric correction errors in the b3 channel. In addition, it makes sense to use the results of the OC2-like algorithms if the b3 range is used to estimate the CDOM content, so as not to strengthen the correlation between the satellite chl-a and CDOM estimations.

The b4 spectral range, which is only available on radiometers belonging to the MODIS family, provided less desirable results; however, they would be acceptable for a rough estimate of chl-a if higher spatial resolution is needed in the era of MODIS radiometers.

Sun-induced fluorescence signals may be an alternative way to calculate chl-a concentration [61,62] in cases with high chl-a values and where uncertainties from the non-constant ratios of chl-a/CDOM exceed uncertainties from the variability of the functional state of phytoplankton cells or their species composition. However, the use of spectral channels from the chl-a fluorescence spectral region is not yet recommended, since there is no certainty that factors unrelated to the concentration of chl-a do not dominate. In addition, closer to the red region of the spectrum, the atmospheric correction errors again begin to increase [51], and the seawater upwelling radiation signal is collected only from the thin near-surface layer of the sea. To introduce a satellite fluorescent bio-optical algorithm for this area, more in situ measurements and the launch of a new generation of satellite radiometers are needed.

5.3. Quality of the Work of Global Bio-Optical Algorithms for Determining the Concentration of Chl-a

From the results presented in Table 8, it can be seen that the global bio-optical algorithms gave acceptable results for their direct application. The *BiasL* values were not very large and became large only for the versions of the algorithms for the OCTS radiometer or the VIIRS/JPSS-1 radiometer. In the first case, the OCTS radiometer may have only worked for a short time in orbit, and the presented version of the global bio-optical algorithm was far from optimal. In the second case, there was a significant difference in *srf* between VIIRS/Suomi-NPP and VIIRS/JPSS-1, because the global algorithm for VIIRS was chosen according to the characteristics of Suomi-NPP. Similar to the regional versions of the algorithms, the global versions using the multi-wavelength OC4 band ratio index provided the best results, both in terms of *R2L* and *MAEL* values. In addition, the spectral characteristics of CZCS gave good results since it uses a channel at 520 nm, which, according to hyperspectral estimates, is optimal for determining the concentration of chl-a in the obtained experimental dataset.

5.4. Recommended Set of Satellite Regional Bio-Optical Algorithms

In general, the global bio-optical algorithms provide acceptable results (Table 8) and thus can be directly used to estimate chl-a concentration. However, based on the results obtained and the discussion, a set of recommended satellite regional bio-optical algorithms is presented here. This will allow for the evaluation of CDOM content, significantly increase the accuracy of determining the concentration of chl-a, and provide recommendations for their use based on the scientific problem being solved.

The results for the OLCI radiometers (OA and OB) and the MODIS radiometers (MA and MT) were combined by averaging the corresponding coefficients, as the differences were insignificant within these families. This does not apply to the VIIRS family, where the differences were found to be significant.

The regional bio-optical algorithms for CDOM content estimation are presented in Table 9; variants using the left blue channel are not included.

The regional bio-optical algorithms for the determination of chl-a concentration are presented in Table 10. For any radiometer, if there is a $R_{OC2}(\lambda_{b6})$ option, then $R_{OC2}(\lambda_{b5})$ should not be used, since it will provide a slightly worse result and it will not have its own separate recommendation for use.

Table 9. Set of satellite regional bio-optical algorithms for the estimation of CDOM content in QSU units (in mg/m³) for the range 0.63–5.31 QSU and related recommendations.

Algorithm Name	Sensor Name	λ_D , nm	λ_{b7} , nm	d_0	d_1	MAEL	R2L
OC2-like algorithms using b2 spectral range in the case of very good atmosphere correction to obtain values independent from chl-a concentrations							
OC2b2-O	OLCI	412	560	0.2362	−0.6992	1.19	0.85
OC2b2-SG	SGLI	412	566	0.2505	−0.6759	1.19	0.84
OC2-like algorithms using b3 spectral range in the case of mediocre atmosphere correction and to estimate the order of magnitude of CDOM content							
OC2b3-CN	CZCS	443	550	0.2141	−0.8531	1.22	0.77
OC2b3-CA	OCTS	443	565	0.2525	−0.7339	1.23	0.74
OC2b3-ME	MERIS	443	560	0.2233	−0.7502	1.23	0.75
OC2b3-O	OLCI	443	560	0.2241	−0.7487	1.23	0.74
OC2b3-M	MODIS	443	547	0.2057	−0.8810	1.22	0.78
OC2b3-SO	SeaWiFS	443	555	0.2218	−0.8147	1.23	0.75
OC2b3-SG	SGLI	443	566	0.2394	−0.7181	1.23	0.74
OC2b3-VS	VIIRS/SNPP	443	551	0.2149	−0.8637	1.22	0.77
OC2b3-VJ	VIIRS/JPSS-1	445	556	0.2222	−0.7937	1.23	0.75

Table 10. Set of satellite regional bio-optical algorithms for the estimation of chl-a concentration in mg/m³ for the range 0.17 to 9.29 mg/m³ and related recommendations.

Algorithm Name	Sensor Name	λ_C , nm	λ_{b7} , nm	c_0	c_1	MAEL	R2L
OC2-like algorithm for MODIS high spatial resolution							
OC2b4-M-HI	MODIS-HI	469	555	0.2077	−1.886	1.5	0.76
OC2-like algorithms in the case of bad atmosphere correction or for values more independent of CDOM content							
OC2b6-CN	CZCS	520	550	0.3231	−5.3564	1.46	0.82
OC2b6-CA	OCTS	516	565	0.4457	−3.3162	1.47	0.81
OC2b6-ME	MERIS	510	560	0.3421	−3.0684	1.46	0.81
OC2b6-O	OLCI	510	560	0.34215	−3.0846	1.46	0.81
OC2b6-M	MODIS	531	547	0.35465	−9.5005	1.45	0.82
OC2b6-SO	SeaWiFS	510	555	0.3498	−3.4623	1.46	0.81
OC2b6-SG	SGLI	529	566	0.4501	−4.3752	1.49	0.8
OC2b5-VS	VIIRS/SNPP	486	551	0.287	−2.4257	1.48	0.79
OC2b5-VJ	VIIRS/JPSS-1	489	556	0.3077	−2.2368	1.47	0.8
OC3-like and OC4-like algorithms for the precise estimation of chl-a concentration in the case of good atmosphere correction							
OC3b6-CN	CZCS	443 > 520	550	0.3316	−2.3556	1.41	0.82
OC4-CA	OCTS	443 > 490 > 516	565	0.4244	−1.994	1.41	0.83
OC4-ME	MERIS	443 > 490 > 510	560	0.354	−2.0469	1.42	0.83
OC4-M	OLCI	443 > 488 > 531	547	0.3603	−2.55815	1.43	0.81
OC4-O	MODIS	443 > 490 > 510	560	0.3552	−2.04175	1.42	0.83
OC4-SO	SeaWiFS	443 > 490 > 510	555	0.3533	−2.2356	1.42	0.83
OC4-SG	SGLI	443 > 490 > 529	566	0.4242	−2.0369	1.41	0.84
OC3b5-VS	VIIRS/SNPP	443 > 486	551	0.2866	−2.1739	1.46	0.8
OC3b5-VJ	VIIRS/JPSS-1	445 > 489	556	0.3057	−2.0126	1.45	0.81

The recommendations given for the use of regional algorithms in Tables 9 and 10 are also valid for global satellite algorithms.

Determining whether the atmospheric correction is satisfactory or not can be achieved by comparing the results of algorithms using channels from the spectral ranges b2, b3, and b5 and analyzing the stability of the obtained characteristics in space and time. In addition, no flags of data processing quality, associated with possible atmospheric correction failures or poor lighting conditions, can be triggered.

It must be kept in mind that the obtained results should not be interpreted as some satellite scanners having less successful spectral characteristics in general or vice versa, because the presented results are regional and seasonal. In other areas of the ocean, this may be a different situation.

6. Conclusions

The following main results obtained in this study on the western part of the Bering Sea can be noted as follows:

- (1) The list of recommended regional bio-optical algorithms for application to satellite ocean color data is presented in Tables 9 and 10.
- (2) It was shown that using channels from the b2 spectral region (404–424 nm) did not provide considerably worse results than using channels from the b1 region (374–403 nm) for the remote sensing estimation of CDOM and to distinguish the contribution of CDOM and phytoplankton to ocean color. Thus, the b2 spectral range is recommended for CDOM content estimation with modern satellite radiometers that have additional bands in the b1 range. In addition, the latter can be used for better atmospheric correction.
- (3) The b3 spectral range (431–454 nm) can be used to estimate the orders of magnitude of CDOM content; however, it cannot be used to derive the independent spatial distributions of CDOM because there is a too high a correlation with chl-a concentration.
- (4) To determine chl-a concentrations from remote sensing data, the best results were provided by the multiwavelength OC3-like and OC4-like algorithms.
- (5) Algorithms from the OC2 family are recommended for determining chl-a in the b5 (476–500 nm) and b6 (501–539 nm) spectral ranges in the case of large atmospheric correction errors. The b6 range may be used to obtain estimates that are more independent of the CDOM content.
- (6) The b4 spectral range (456–475) is not very good for determining chl-a concentration but is acceptable if the use of high spatial resolution MODIS data is required.
- (7) The global bio-optical algorithms provide acceptable results (Table 8) and can be directly used to estimate chl-a concentration with the same recommendations as those for the regional bio-optical algorithms.

However, this does not mean that the same results will be observed in other areas and seasons. The obtained results show an improvement in the accuracy of determining the concentration of chl-a and CDOM in the waters of the western part of the Bering Sea with a non-constant ratio between these two OACs. This makes it possible to select the initial and boundary conditions for semi-analytical approaches as accurately as possible, or in some cases avoid the need to use them.

Author Contributions: Conceptualization, P.A.S. and I.E.S.; methodology, P.A.S., I.E.S. and V.A.K.; software, P.A.S., I.E.S. and V.A.K.; validation, E.B.S., S.P.P. and I.I.P.; formal analysis, P.A.S., I.E.S., S.P.P. and I.I.P.; investigation, P.A.S., I.E.S. and E.B.S.; resources, P.A.S.; data curation, P.A.S., I.E.S. and V.A.K.; writing—original draft preparation, P.A.S.; writing—review and editing, E.B.S.; visualization, P.A.S. and I.E.S.; supervision, P.A.S.; project administration, P.A.S.; funding acquisition, P.A.S., S.P.P. and I.I.P. All authors have read and agreed to the published version of the manuscript.

Funding: This complex work was supported by the Russian state budget theme 0211-2021-0007 (field data collection and processing), Russian Foundation of Basic Research (grant No. 20-05-00545, bio-optical model development), Russian Science Foundation (grant No. 21-17-00027, analysis of water masses and sources of CDOM), Russian Science Foundation (grant No. 21-77-10059, analysis of CDOM influence on remote sensing estimations of chl-a concentrations), Far Eastern State University (Project Prioritet-2030, above-water remote sensing data processing), and by the Federal Science and Technology Programme of the Russian Federation in the areas of environmental improvement and climate change for 2021–2030 within the project «Rationale for the Climate Monitoring System of the Far Eastern seas and Development of Methods for Monitoring Extreme Weather and Climate Ocean-Related Phenomena Based on Stationary and Mobile Measuring Complexes, as well as Multi-Sensor Satellite Sensing» (the list of regional bio-optical algorithms and satellite data processing).

Data Availability Statement: The satellite ocean color data can be found on Ocean Color Web (<https://oceancolor.gsfc.nasa.gov/cgi/browse.pl?sen=amod>, accessed on 15 November 2022), where Level 2 data from MODIS/Aqua [63], MODIS/Terra [64] and VIIRS/Suomi-NPP [65] radiometers were used. The author’s ship data are available upon request.

Acknowledgments: The authors are sincerely grateful to the crew of the “Professor Khiljustin” ship and the head of the expedition Oleg A. Bukin. Special thanks to Mikhail S. Permyakov from POI FEB RAS for the valuable comments and advice.

Conflicts of Interest: The authors declare no conflict of interest.

References

- O’Reilly, J.E.; Maritorena, S.; Mitchell, B.G.; Siegel, D.A.; Carder, K.L.; Garver, S.A.; Kahru, M.; McClain, C. Ocean color chlorophyll algorithms for SeaWiFS. *J. Geophys. Res. Ocean.* **1998**, *103*, 24937–24953. [CrossRef]
- Matthews, M.W. A current review of empirical procedures of remote sensing in inland and near-coastal transitional waters. *Int. J. Remote Sens.* **2011**, *32*, 6855–6899. [CrossRef]
- Werdell, P.J.; McKinna, L.I.; Boss, E.; Ackleson, S.G.; Craig, S.E.; Gregg, W.W.; Lee, Z.; Maritorena, S.; Roesler, C.S.; Rousseaux, C.S.; et al. An overview of approaches and challenges for retrieving marine inherent optical properties from ocean color remote sensing. *Prog. Oceanogr.* **2018**, *160*, 186–212. [CrossRef] [PubMed]
- Blondeau-Patissier, D.; Gower, J.F.R.; Dekker, A.G.; Phinn, S.R.; Brando, V.E. A review of ocean color remote sensing methods and statistical techniques for the detection, mapping and analysis of phytoplankton blooms in coastal and open oceans. *Prog. Oceanogr.* **2014**, *123*, 123–144. [CrossRef]
- Brewin, R.J.W.; Raitos, D.E.; Dall’Omo, G.; Zarokanellos, N.; Jackson, T.; Racault, M.-F.; Boss, E.S.; Sathyendranath, S.; Jones, B.H.; Hoteit, I. Regional ocean-colour chlorophyll algorithms for the Red Sea. *Remote Sens. Environ.* **2015**, *165*, 64–85. [CrossRef]
- Ogashawara, I.; Mishra, D.R.; Nascimento, R.F.F.; Alcântara, E.H.; Kampel, M.; Stech, J.L. Re-parameterization of a quasi-analytical algorithm for colored dissolved organic matter dominant inland waters. *Int. J. Appl. Earth Obs. Geoinf.* **2016**, *53*, 128–145. [CrossRef]
- Darecki, M.; Stramski, D. An evaluation of MODIS and SeaWiFS bio-optical algorithms in the Baltic Sea. *Remote Sens. Environ.* **2004**, *89*, 326–350. [CrossRef]
- Gregg, W.W.; Casey, N.W. Global and regional evaluation of the SeaWiFS chlorophyll data set. *Remote Sens. Environ.* **2004**, *93*, 463–479. [CrossRef]
- Siswanto, E.; Tang, J.; Yamaguchi, H.; Ahn, Y.-H.; Ishizaka, J.; Yoo, S.; Kim, S.-W.; Kiyomoto, Y.; Yamada, K.; Chiang, C.; et al. Empirical ocean-color algorithms to retrieve chlorophyll-a, total suspended matter, and colored dissolved organic matter absorption coefficient in the Yellow and East China Seas. *J. Oceanogr.* **2011**, *67*, 627–650. [CrossRef]
- Suslin, V.; Churilova, T. A regional algorithm for separating light absorption by chlorophyll- a and coloured detrital matter in the Black Sea, using 480–560 nm bands from ocean colour scanners. *Int. J. Remote Sens.* **2016**, *37*, 4380–4400. [CrossRef]
- Kopelevich, O.V.; Burenkov, V.I.; Ershova, S.V.; Sheberstov, S.V.; Evdoshenko, M.A. Application of SeaWiFS data for studying variability of bio-optical characteristics in the Barents, Black and Caspian Seas. *Deep Sea Res. Part II Top. Stud. Oceanogr.* **2004**, *51*, 1063–1091. [CrossRef]
- Salyuk, P.A.; Bukin, O.A.; Aleksanin, A.I.; Pavlov, A.N.; Mayor, A.Y.; Shmirko, K.A.; Akmaykin, D.A.; Krikun, V.A. Optical properties of Peter the Great Bay waters compared with satellite ocean colour data. *Int. J. Remote Sens.* **2010**, *31*, 4651–4664. [CrossRef]
- Rehm, E.; Mobley, C.D. Estimation of hyperspectral inherent optical properties from in-water radiometry: Error analysis and application to in situ data. *Appl. Opt.* **2013**, *52*, 795–817. [CrossRef] [PubMed]
- Sathyendranat, S. (Ed.) Remote Sensing of Ocean Colour in Coastal, and Other Optically-Complex, Waters. In *Reports of the International Ocean-Colour Coordinating Group*; IOCCG: Dartmouth, NS, Canada, 2000; Volume 3.
- Morel, A.; Prieur, L. Analysis of variations in ocean color1. *Limnol. Oceanogr.* **1977**, *22*, 709–722. [CrossRef]

16. Bukin, O.A.; Salyuk, P.A.; Maior, A.Y.; Pavlov, A.N. Studies of organic matter reproduction in phytoplankton cells by laser-induced fluorescence method. *Atmos. Ocean. Opt.* **2005**, *18*, 871–878.
17. Morel, A.; Gentili, B. A simple band ratio technique to quantify the colored dissolved and detrital organic material from ocean color remotely sensed data. *Remote Sens. Environ.* **2009**, *113*, 998–1011. [[CrossRef](#)]
18. O'Reilly, J.E.; Werdell, P.J. Chlorophyll algorithms for ocean color sensors—OC4, OC5 & OC6. *Remote Sens. Environ.* **2019**, *229*, 32–47. [[CrossRef](#)]
19. NASA Ocean Color Web. Available online: <https://oceancolor.gsfc.nasa.gov> (accessed on 20 October 2022).
20. Copernicus Marine Environment Monitoring Service (CMEMS), Global Ocean Physics Reanalysis. Available online: https://data.marine.copernicus.eu/product/GLOBAL_MULTIYEAR_PHY_001_030/description (accessed on 20 October 2022). [[CrossRef](#)]
21. Naik, P.; D'Sa, E.J.; Gomes, H.d.; Goés, J.I.; Mouw, C.B. Light absorption properties of southeastern Bering Sea waters: Analysis, parameterization and implications for remote sensing. *Remote Sens. Environ.* **2013**, *134*, 120–134. [[CrossRef](#)]
22. Naik, P.; Wang, M.; D'Sa, E.J.; Mordy, C.W. Bering Sea optical and biological properties from MODIS. *Remote Sens. Environ.* **2015**, *163*, 240–252. [[CrossRef](#)]
23. Fujiwara, A.; Hirawake, T.; Suzuki, K.; Saitoh, S.-I. Remote sensing of size structure of phytoplankton communities using optical properties of the Chukchi and Bering Sea shelf region. *Biogeosciences* **2011**, *8*, 3567–3580. [[CrossRef](#)]
24. Sasaki, H.; Saitoh, S.-I.; Kishino, M. Bio-Optical Properties of Seawater in the Western Subarctic Gyre and Alaskan Gyre in the Subarctic North Pacific and the Southern Bering Sea during the Summer of 1997. *J. Oceanogr.* **2001**, *57*, 275–284. [[CrossRef](#)]
25. Salyuk, P.A.; Stepochkin, I.E.; Bukin, O.A.; Sokolova, E.B.; Mayor, A.Y.; Shambarova, J.V.; Gorbushkin, A.R. Determination of the chlorophyll a concentration by MODIS-Aqua and VIIRS satellite radiometers in Eastern Arctic and Bering Sea. *Izv. Atmos. Ocean. Phys.* **2016**, *52*, 988–998. [[CrossRef](#)]
26. Hirawake, T.; Oida, J.; Yamashita, Y.; Waga, H.; Abe, H.; Nishioka, J.; Nomura, D.; Ueno, H.; Ooki, A. Water mass distribution in the northern Bering and southern Chukchi seas using light absorption of chromophoric dissolved organic matter. *Prog. Oceanogr.* **2021**, *197*, 102641. [[CrossRef](#)]
27. Clement, J.L.; Maslowski, W.; Cooper, L.W.; Grebmeier, J.M.; Walczowski, W. Ocean circulation and exchanges through the northern Bering Sea—1979–2001 model results. *Deep Sea Res. Part II Top. Stud. Oceanogr.* **2005**, *52*, 3509–3540. [[CrossRef](#)]
28. Danielson, S.L.; Weingartner, T.J.; Hedstrom, K.S.; Aagaard, K.; Woodgate, R.; Curchitser, E.; Stabeno, P.J. Coupled wind-forced controls of the Bering–Chukchi shelf circulation and the Bering Strait throughflow: Ekman transport, continental shelf waves, and variations of the Pacific–Arctic sea surface height gradient. *Prog. Oceanogr.* **2014**, *125*, 40–61. [[CrossRef](#)]
29. Danielson, S.L.; Eisner, L.; Ladd, C.; Mordy, C.; Sousa, L.; Weingartner, T.J. A comparison between late summer 2012 and 2013 water masses, macronutrients, and phytoplankton standing crops in the northern Bering and Chukchi Seas. *Deep Sea Res. Part II Top. Stud. Oceanogr.* **2017**, *135*, 7–26. [[CrossRef](#)]
30. Stabeno, P.J.; Danielson, S.L.; Kachel, D.G.; Kachel, N.B.; Mordy, C.W. Currents and transport on the Eastern Bering Sea shelf: An integration of over 20 years of data. *Deep Sea Res. Part II Top. Stud. Oceanogr.* **2016**, *134*, 13–29. [[CrossRef](#)]
31. Nishioka, J.; Hirawake, T.; Nomura, D.; Yamashita, Y.; Ono, K.; Murayama, A.; Shcherbinin, A.; Volkov, Y.N.; Mitsudera, H.; Ebuchi, N.; et al. Iron and nutrient dynamics along the East Kamchatka Current, western Bering Sea Basin and Gulf of Anadyr. *Prog. Oceanogr.* **2021**, *198*, 102662. [[CrossRef](#)]
32. Pipko, I.I.; Pugach, S.P.; Savelieva, N.I.; Luchin, V.A.; Dudarev, O.V.; Sergienko, V.I.; Semiletov, I.P. Carbonate characteristics of the Gulf of Anadyr waters. *Dokl. Earth Sci.* **2019**, *487*, 867–871. [[CrossRef](#)]
33. Pipko, I.I.; Pugach, S.P.; Luchin, V.A.; Francis, O.P.; Savelieva, N.I.; Charkin, A.N.; Dudarev, O.V.; Semiletov, I.P. Surface CO₂ system dynamics in the Gulf of Anadyr during the open water season. *Cont. Shelf Res.* **2021**, *217*, 104371. [[CrossRef](#)]
34. Nomura, D.; Abe, H.; Hirawake, T.; Ooki, A.; Yamashita, Y.; Murayama, A.; Ono, K.; Nishioka, J. Formation of dense shelf water associated with sea ice freezing in the Gulf of Anadyr estimated with oxygen isotopic ratios. *Prog. Oceanogr.* **2021**, *196*, 102595. [[CrossRef](#)]
35. Nagorny, I.G.; Salyuk, P.A.; Maior, A.Y.; Doroshenko, I.M. A mobile complex for on-line studying water areas and surface atmosphere. *Instrum. Exp. Tech.* **2014**, *57*, 68–71. [[CrossRef](#)]
36. Salyuk, P.A.; Podoprighora, E.L. Comparative analysis of the chlorophyll A concentrations obtained by the laser-induced fluorescence method (LIF) and SeaWiFS. *SPIE Proc. Laser Appl. Med. Biol. Environ. Sci.* **2003**, *5149*, 53–59. [[CrossRef](#)]
37. Smith, R.C.; Baker, K.S. Optical properties of the clearest natural waters (200–800 nm). *Appl. Opt.* **1981**, *20*, 177–184. [[CrossRef](#)] [[PubMed](#)]
38. De Moraes Rudorff, N.; Frouin, R.; Kampel, M.; Goyens, C.; Meriaux, X.; Schieber, B.; Mitchell, B.G. Ocean-color radiometry across the Southern Atlantic and Southeastern Pacific: Accuracy and remote sensing implications. *Remote Sens. Environ.* **2014**, *149*, 13–32. [[CrossRef](#)]
39. Mueller, J.L.; Morel, A.; Frouin, R.; Davis, C.; Arnone, R.; Carder, K.; Lee, Z.P.; Steward, R.G.; Hooker, S.; Mobley, C.D.; et al. Radiometric Measurements and Data Analysis Protocols. In *Ocean Optics Protocols For Satellite Ocean Colour Sensor Validation*; Revision 4; Goddard Space Flight Space Centre: Greenbelt, MD, USA, 2003; Volume 3.
40. Ruddick, K.G.; Ovidio, F.; Rijkeboer, M. Atmospheric correction of SeaWiFS imagery for turbid coastal and inland waters. *Appl. Opt.* **2000**, *39*, 897–912. [[CrossRef](#)]
41. Mobley, C.D. Estimation of the remote-sensing reflectance from above-surface measurements. *Appl. Opt.* **1999**, *38*, 7442–7455. [[CrossRef](#)]

42. Morel, A.; Mueller, J.L. Normalized Water-Leaving Radiance and Remote Sensing Reflectance: Bidirectional Reflectance and Other Factors. In *Ocean Optics Protocols for Satellite Ocean Colour Sensor Validation*; Revision 3; Mueller, J.L., Fargion, G.S., Eds.; Goddard Space Flight Space Centre: Greenbelt, MD, USA, 2002; Volume 2, pp. 183–210.
43. Zibordi, G.; Ruddick, K.; Ansko, I.; Moore, G.; Kratzer, S.; Icely, J.; Reinart, A. In situ determination of the remote sensing reflectance: An inter-comparison. *Ocean Sci.* **2012**, *8*, 567–586. [[CrossRef](#)]
44. NASA Ocean Color Web, Response Spectral Function Data. Available online: https://oceancolor.gsfc.nasa.gov/docs/rsr/rsr_tables/ (accessed on 20 October 2022).
45. O'Reilly, J.E.; Maritorena, S.; O'Brien, M.C.; Siegel, D.A.; Toole, D.; Menzies, D.; Smith, R.C.; Mueller, J.L.; Mitchell, B.G.; Kahru, M.; et al. SeaWiFS postlaunch calibration and validation analyses. In *SeaWiFS Postlaunch Technical Report Series*; Hooker, S.B., Firestone, E.R., Eds.; Goddard Space Flight Space Centre: Greenbelt, MD, USA, 2000; Volume 11, Part 3; 49p.
46. NASA Ocean Color Web, Chlor_a Product Description. Available online: https://oceancolor.gsfc.nasa.gov/atbd/chlor_a/ (accessed on 20 October 2022).
47. Seegers, B.N.; Stumpf, R.P.; Schaeffer, B.A.; Loftin, K.A.; Werdell, P.J. Performance metrics for the assessment of satellite data products: An ocean color case study. *Opt. Express* **2018**, *26*, 7404–7422. [[CrossRef](#)]
48. Efron, B. *The Jackknife, The Bootstrap and Other Resampling Plans*; The Society for Industrial and Applied Mathematics: Philadelphia, PA, USA, 1982.
49. Kleshcheva, T.I.; Permyakov, M.S.; Salyuk, P.A.; Golik, I.A. Wavenumber spectra of the chlorophyll “a” concentration and the sea surface temperature in the area of the anticyclonic eddy in the South China Sea. *J. Oceanogr.* **2021**, *77*, 259–267. [[CrossRef](#)]
50. Bukin, O.A.; Permyakov, M.S.; Maior, A.Y.; Sagalaev, S.G.; Lipilina, E.A.; Khovanets, V.A. Calibration of the method of laser fluorometry for measuring the chlorophyll A concentration. *Atmos. Ocean. Opt.* **2001**, *14*, 203–206. Available online: <http://ao.iao.ru/en/content/text?vol=14&issue=03&num=8> (accessed on 10 November 2022).
51. Aleksanin, A.I.; Kachur, V.A. Specificity of Atmospheric Correction of Satellite Data on Ocean Color in the Far East. *Izv. Atmos. Ocean. Phys.* **2017**, *53*, 996–1006. [[CrossRef](#)]
52. Kim, W.; Moon, J.-E.; Park, Y.-J.; Ishizaka, J. Evaluation of chlorophyll retrievals from Geostationary Ocean Color Imager (GOCI) for the North-East Asian region. *Remote Sens. Environ.* **2016**, *184*, 482–495. [[CrossRef](#)]
53. Huot, Y.; Franz, B.A.; Fradette, M. Estimating variability in the quantum yield of Sun-induced chlorophyll fluorescence: A global analysis of oceanic waters. *Remote Sens. Environ.* **2013**, *132*, 238–253. [[CrossRef](#)]
54. Behrenfeld, M.J.; Westberry, T.K.; Boss, E.S.; O'Malley, R.T.; Siegel, D.A.; Wiggert, J.D.; Franz, B.A.; McClain, C.R.; Feldman, G.C.; Doney, S.C.; et al. Satellite-detected fluorescence reveals global physiology of ocean phytoplankton. *Biogeosciences* **2009**, *6*, 779–794. [[CrossRef](#)]
55. Oudrari, H.; McIntire, J.; Xiong, X.; Butler, J.; Ji, Q.; Schwarting, T.; Lee, S.; Efremova, B. JPSS-1 VIIRS Radiometric Characterization and Calibration Based on Pre-Launch Testing. *Remote Sens.* **2016**, *8*, 41. [[CrossRef](#)]
56. Barnes, B.B.; Cannizzaro, J.P.; English, D.C.; Hu, C. Validation of VIIRS and MODIS reflectance data in coastal and oceanic waters: An assessment of methods. *Remote Sens. Environ.* **2019**, *220*, 110–123. [[CrossRef](#)]
57. Oo, M.; Vargas, M.; Gilerson, A.; Gross, B.; Moshary, F.; Ahmed, S. Improving atmospheric correction for highly productive coastal waters using the short wave infrared retrieval algorithm with water-leaving reflectance constraints at 412 nm. *Appl. Opt.* **2008**, *47*, 3846–3859. [[CrossRef](#)]
58. Emberton, S.; Chittka, L.; Cavallaro, A.; Wang, M. Sensor Capability and Atmospheric Correction in Ocean Colour Remote Sensing. *Remote Sens.* **2016**, *8*, 1. [[CrossRef](#)]
59. Mognane, M.; Jamet, C.; Loisel, H.; Vantrepotte, V.; Mériaux, X.; Cauvin, A. Evaluation of Five Atmospheric Correction Algorithms over French Optically-Complex Waters for the Sentinel-3A OLCI Ocean Color Sensor. *Remote Sens.* **2019**, *11*, 668. [[CrossRef](#)]
60. Wang, M.; Jiang, L. Atmospheric Correction Using the Information from the Short Blue Band. *IEEE Trans. Geosci. Remote Sens.* **2018**, *56*, 6224–6237. [[CrossRef](#)]
61. Gower, J.; King, S. Validation of chlorophyll fluorescence derived from MERIS on the west coast of Canada. *Int. J. Remote Sens.* **2007**, *28*, 625–635. [[CrossRef](#)]
62. Huot, Y.; Brown, C.A.; Cullen, J.J. New algorithms for MODIS sun-induced chlorophyll fluorescence and a comparison with present data products. *Limnol. Oceanogr. Methods* **2005**, *3*, 108–130. [[CrossRef](#)]
63. NASA Goddard Space Flight Center, Ocean Ecology Laboratory, Ocean Biology Processing Group. *Moderate-Resolution Imaging Spectroradiometer (MODIS) Aqua Ocean Color Data*; 2022 Reprocessing; NASA OB.DAAC: Greenbelt, MD, USA.
64. NASA Goddard Space Flight Center, Ocean Ecology Laboratory, Ocean Biology Processing Group. *Moderate-Resolution Imaging Spectroradiometer (MODIS) Terra Ocean Color Data*; 2018 Reprocessing; NASA OB.DAAC: Greenbelt, MD, USA.
65. NASA Goddard Space Flight Center, Ocean Ecology Laboratory, Ocean Biology Processing Group. *Visible and Infrared Imager/Radiometer Suite (VIIRS) Ocean Color Data*; 2022 Reprocessing; NASA OB.DAAC: Greenbelt, MD, USA.